AIMS Geosciences, 6(3): 316–354.
DOI: 10.3934/geosci.2020019
Received: 25 June 2020
Accepted: 17 August 2020
Published: 08 September 2020

http://www.aimspress.com/journal/geosciences

Research article

Geochemistry, facies characteristics and palaeoenvironmental conditions of the storm-dominated phosphate-bearing deposits of eastern Tethyan Ocean; A case study from Zagros region, SW Iran

Armin Salsani[1], Abdolhossein Amini[2,*], Shahram shariati[3], Seyed Ali Aghanabati[4] and Mohsen Aleali[1]

[1] Department of Geology, Science and Research Branch, Islamic Azad University, Tehran, Iran
[2] School of Geology, College of Science, University of Tehran, Tehran, Iran
[3] Department of Geology, Sari branch, Islamic Azad University, Sari, Iran
[4] Earth Sciences Research Institute, Geological Survey of Iran, Tehran, Iran

* **Correspondence:** Email: ahamini@ut.ac.ir; Tel: +989123435080; Fax: +982122362408.

Abstract: Phosphate deposits in south-western Iran are part of the South Tethyan Phosphogenic Province, a huge carbonate-dominated strata that extends to the Middle East. The Tethyan phosphorites of Iran are dated Eocene-Oligocene (Pabdeh Formation) and categorized as low-grade ore deposits on a global scale. Depositional conditions of the facies indicate that the Pabdeh Formation was deposited on a carbonate ramp setting as a distally steepened ramp. Under such an environment, turbidity currents transported phosphate particles from the back-shoal setting to the deeper middle and outer ramp of the ocean where they were suspended and deposited as shell-lag and phosphate lamination. Microfacies studies demonstrate that all the phosphatic ooids and phosphatized foraminifera, fish scales, bones and phosphatic intraclasts reworked from shallow parts of the Tethyan Ocean to deeper parts with the help of turbidity currents. Analysis and interpretation of the data reveal positive correlation between. REE+Y and P_2O_5 in all studied sections which attests to their strong coherence as a geochemical group. The shale normalized REE patterns of Mondun phosphorites are characterized by negative Ce anomalies. This anomaly indicate that the depositional environment was oxic and highly reworked, bioturbated with higher energy realm during phosphate deposition, conversely Nill section with Ce enrichment reflect conditions of relatively deeper water sedimentation. These geochemical findings are in accordance with microfacies studies which indicate shallow and high energy condition for

Mondun section with negative cerium anomalies and a deep ramp setting for Nill and Siah sections which denote a positive cerium anomalies in REE patterns.

Keywords: Tethyan phosphorites; Pabdeh Formation; shell-lag; turbidity currents; rare-earth elements and yttrium

1. Introduction

The Zagros fold and thrust belt extends from south Turkey through Iraq to southwest Iran and is about 1800 km long and 150 km wide. The belt is associated with a foreland basin and represents the oldest and richest hydrocarbon zone in the area [1]. The late Palaeocene to early Oligocene Pabdeh Formation and the underlying Gurpi Formation are known for their potential oil reserves. The Pabdeh Formation, with a thin (1–3 m), purple, sandy to silty shale at the base, overlies a highly weathered, glauconitic-rich layer (the top of the Gurpi Formation) which indicates a significant unconformity [2]. Palaeontological data suggests a missing period of about 10 my for this unconformity [3].

The Pabdeh Formation in the study area consists of thin- to thick-bedded limestones alternating with dark to light grey shales and green to grey marls, rich in planktonic microfauna. In most parts of the Zagros, especially in the Dezful embayment, this formation is described as a fine-grained, matrix-rich, carbonate-dominated succession with some hydrocarbon source potential [4–6]. Although many studies have been carried out on its potential oil reserves, the Pabdeh Formation has rarely been investigated for its phosphate bearing horizons.

This study investigates the facies characteristics, precise potential and depositional conditions of the phosphate-bearing horizons of the Pabdeh formation in the best outcrops of the Zagros region. We reconstruct the depositional environment of the Pabdeh Formation with emphasis on the phosphate and non-phosphate horizons using microfacies studies and sedimentary, geochemical and fossil evidence. This study focuses on the phosphate-bearing horizons of the Pabdeh formation and presents the first fully integrated geochemical study of the Pabdeh Formation, highlighting the key similarities and differences between the phosphate-bearing horizons. This work addresses the abundances of major, trace, and rare-earth elements, their distribution patterns and inter-element relationships.

2. Geological setting and stratigraphy

The NW–SE trending Mountains of west and southwest Iran are parts of the Alpine–Himalayan orogenic belt, known as the Zagros belt [7]. The Zagros belt represents the NE margin of the Arabian plate, in which discontinuous deposition occurred from the very late Precambrian to the Late Miocene [2,8]. This fold and thrust belt is a result of the structural deformation of the Zagros (peripheral) proforeland system, whose present-day expression is the marine Persian Gulf and continental Mesopotamia basins [9–12], and the underlying preproforeland, mostly platformal and continental shelf deposits. The closure is related to the Arabian Plate subduction beneath the Central Iran block that was formed in the Late Cretaceous [2,8,13,14]. Subsequently, the collisional mountain-building that began in the Middle Maastrichtian (about 68 Ma) has continued with variable intensity until recently [2]. This collision led to the closure of the Neo-Tethys basin and the formation of the Zagros foreland basin with a sedimentary record from the Late Cretaceous until recently [15]. The

deep-marine Pabdeh Formation with hemipelagic-pelagic calcareous shale, marl, and lime mudstone with subordinate argillaceous limestone was deposited in the Zagros proforeland basin during the Early Eocene to Oligocene. Most studies relate the depositional environment of the formation to a ramp setting [16–19]. Evidence of a deep marine environment [20] and pelagic conditions with common gravity flows [21] can be observed in places (Figure 1).

Mohseni and Al-Aasm [17] and Mohseni et al. [18] found evidence of marine currents and storm deposition during the late depositional stages of the Pabdeh Formation. Moreover, some carbonate tempestites were reported in the stratigraphic record of the formation [17,22–30].

In Iran, the Tethyan phosphorites are restricted to the Eocene-Oligocene Pabdeh Formation. The phosphatic layers of the Pabdeh Formation are categorized as a low-grade ore deposits in the world. The average grade of phosphate in Pabdeh is 8–12% P_2O_5 whereas the average grade of Tethyan phosphorite deposits is 25–30%.

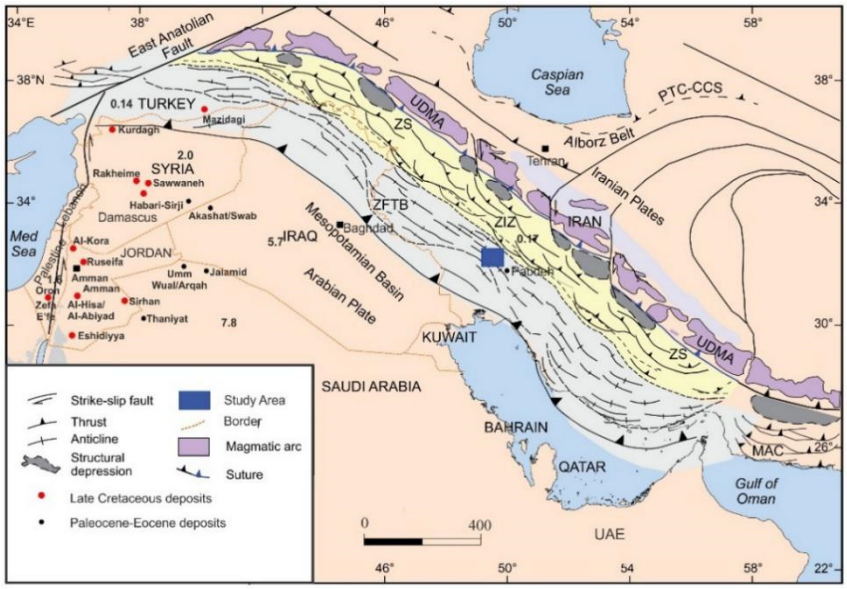

Figure 1. Location of the major phosphorite deposits in the eastern Mediterranean region and adjacent countries, their ages and total resources (bold numbers in billion tonnes) [31]. Subdivisions of the Zagros Orogenic Belt. (Modified from [15]). PTC-CCS = Paleo-Tethyan continent-continent collisional suture; UDMA = Uremiah-Dokhtar Magmatic Assemblage; ZFTB = Zagros Fold-and-Thrust Belt; ZIZ = Zagros Imbricate Zone; ZS = Zagros Suture; MAC = Makran Accretionary Prism.

The eastern Mediterranean region and North Africa hold more than half the world's phosphorite resources, amounting to about 80 billion tonnes of high-grade commercial phosphorites [32–34]. These deposits form part of the Late Cretaceous to Eocene Tethyan Phosphorite Regime that extends through North and northwest Africa, and into parts of the Caribbean and Columbia and Venezuela in northern South America [31,35–39]. These tectonic activities were responsible for setting the scene for the formation of the major phosphorite deposits in the eastern Mediterranean region and throughout the Tethys realm [31]. The Pabdeh Formation is related to Mediterranean phosphatic belt formations such as the Akashat in Iraq [40], Jalamid, Mira and Umm Wu'al and Dammam in Saudi Arabia, Sawwaneh,

Rmah and Bardeh in Syria, Mishash (Palestine), Thelja (Tunisia), Vilga, Abu tarbur, Al-Hisa (Jordan) and Usfan (Saudi Arabia) (Figure 1).

The Akashat Formation is predominantly exposed in the western parts of the Iraq. This Formation, consists of alternation of grey phosphorites and limestones [41] with phosphatic conglomerate or breccia. Depositional environment indicates inner to outer shelf, under subtidal and warm conditions.

The type locality of the Dammam Formation is on the Dammam dome in Saudi Arabia [40]. This Formation which was revealed by Bramkamp [42] consist of sequence of shallow water shelf carbonates interbedded with marls.

Economic phosphorites of Palestine are concentrated in the upper part of the Mishash Formation. The Mishash Formation is of late Campanian in age and forms the uppermost part of a shallow marine epicontinental sediments in Negev region of Palestine phosphorites [43,44].

Tunisia is one of the largest producers of rock phosphate in the world. In Tunisia, significant deposits of phosphorites are found in the Gafsa basin dated Paleocene to early Eocene [45]. The sedimentary rocks are of the Metlaoui group [46], specifically the Thelja Formation [47] which is overlain by the Chouabine Formation and overlies the El Haria Formation [46] (Figure 2). The Ypresian Chouabine Formation contains massive phosphorite layers which alternate with marly limestone, marls and silica-rich layers [48–53]. Sedimentation in the Gafsa-Metlaoui Basin occurred in a relatively restricted setting, which fluctuated between littoral and lagoonal conditions, resulting in rhythmic or episodic sedimentation [52,53]. The Thelja Formation is made up of shallowing-upwards, evaporitic cycles. The Thelja Formation series forms a pattern of nine principal facies that show a gradual transition from offshore marine facies to Sebkha facies with no slope deposits along a gentle inclined platform [54] (Figure 2).

Phosphate deposits in south-western Iran are part of the South Tethyan Phosphogenic Province (STPP), a huge carbonate-dominated Upper Cretaceous to Eocene phosphorite strata that extends from Colombia, through Venezuela, north and northwest Africa to the Middle East [37].

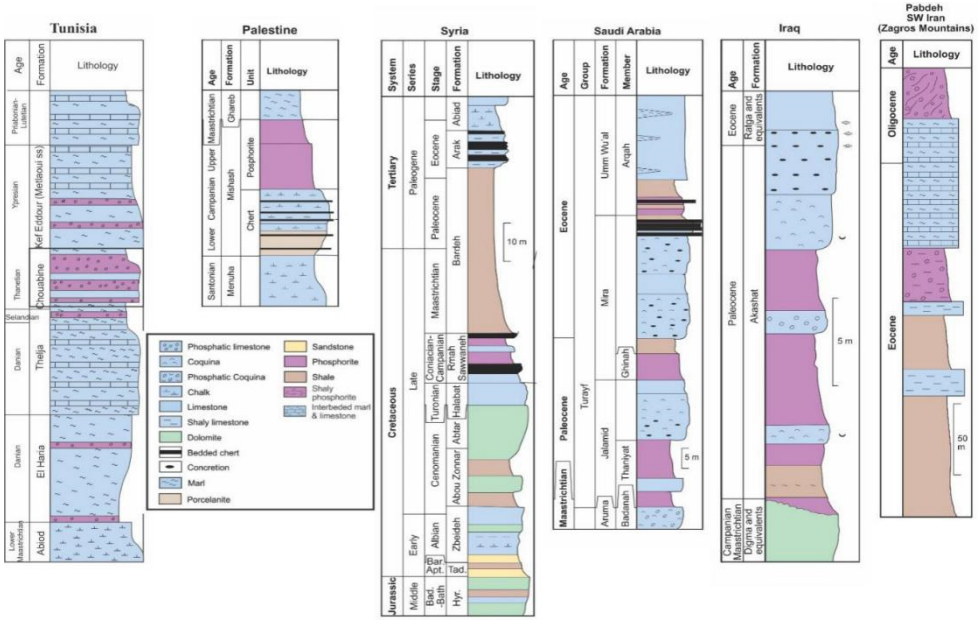

Figure 2. Lithostratigraphy of the Paleocene-Oligocene phosphate bearing horizons of Iraq, Iran, Syria, Saudi Arabia, Tunisia and Palestine (Modified from [31]).

High-grade phosphorites in Syria are limited to the southeastern parts. Rmah Formation is composed of fossiliferous interbedded marl, limestone, dolomite and some chert nodules, overlain by alternations of bedded chert, limestone and thin phosphorite units. Sawwaneh Formation contains the major Syrian phosphorite deposits. The formation consists of marly limestone interbedded with phosphorites.The upper part of the formation is dominated by marl and marly limestone overlain by a glauconitic-phosphatic marl.

Phosphate deposits in northern Saudi Arabia occur in Hazm El-Jalamid, Mira, and Umm Wu'al Formations of the Turayf Group (Paleocene and middle Eocene) (Figure 2). The total thicknesses of the phosphorite beds range between 3 m and 5 m, with up to seven discrete beds [55]. Sedimentary facies analysis of the Hazm Al-Jalamid phosphorites suggests that these phosphorites represent transgressive lag deposits that accumulated in an oxic, bioturbated, and wave dominated shelf environment that developed as a result of the Campanian transgressions of Tethys [56].

The above information suggests that in contrast to the eastern Mediterranean region and north and northwest Africa, where phosphate deposits formed in shallow marine depositional environments and evaporitic cycles, the phosphate horizons of the Pabdeh Formation were formed in a deep marine environment. The condition is in accordance with palaeogeographic map of Tethyan Phosphorite Regime which extends through the eastern Mediterranean region to north and northwest Africa (Figure 3).

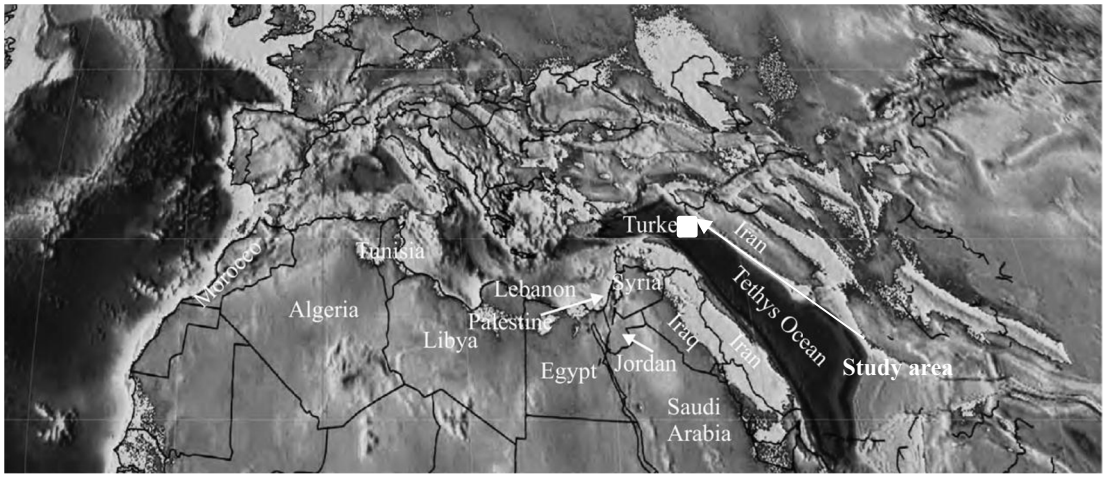

Figure 3. Palaeogeographic map of the Early middle Eocene (44.5 Ma—Middle Lutetian) illustrating the span of the Tethyan ocean. The Tethyan Phosphorite Regime extends through the eastern Mediterranean region to north and northwest Africa. Black lines indicate country boundaries [57].

The study area is located in the Zagros fold and contains the best outcrops of the Pabdeh Formation. Three sections (Nil, Siah and Moundun) of the formation with a total thickness of 1122 m were investigated in this study (Figure 4). In the Nil anticline (115 km north of the city of Gachsaran), the formation consists mainly of interbedded thin to medium limestone, marl and dark grey shale with a total thickness of 512 m. In the Siah Anticline (60 km north of Gachsaran) the formation consists of thin to medium bedded limestone interbedded with shale and marl with a total thickness of 255 m. The Pabdeh Formation at the Mondun Section (85 km north of Gachsaran) is 355 m thick and consists of interbedded limestone and marl at the base and interbedded shale, marl and thin bedded limestone at

the middle to top of the formation. The formation is Early Eocene to Oligocene in age and is overlain by the Oligo-Miocene Asmari Formation and lies above the late Cretaceous Gurpi Formation in the studied sections.

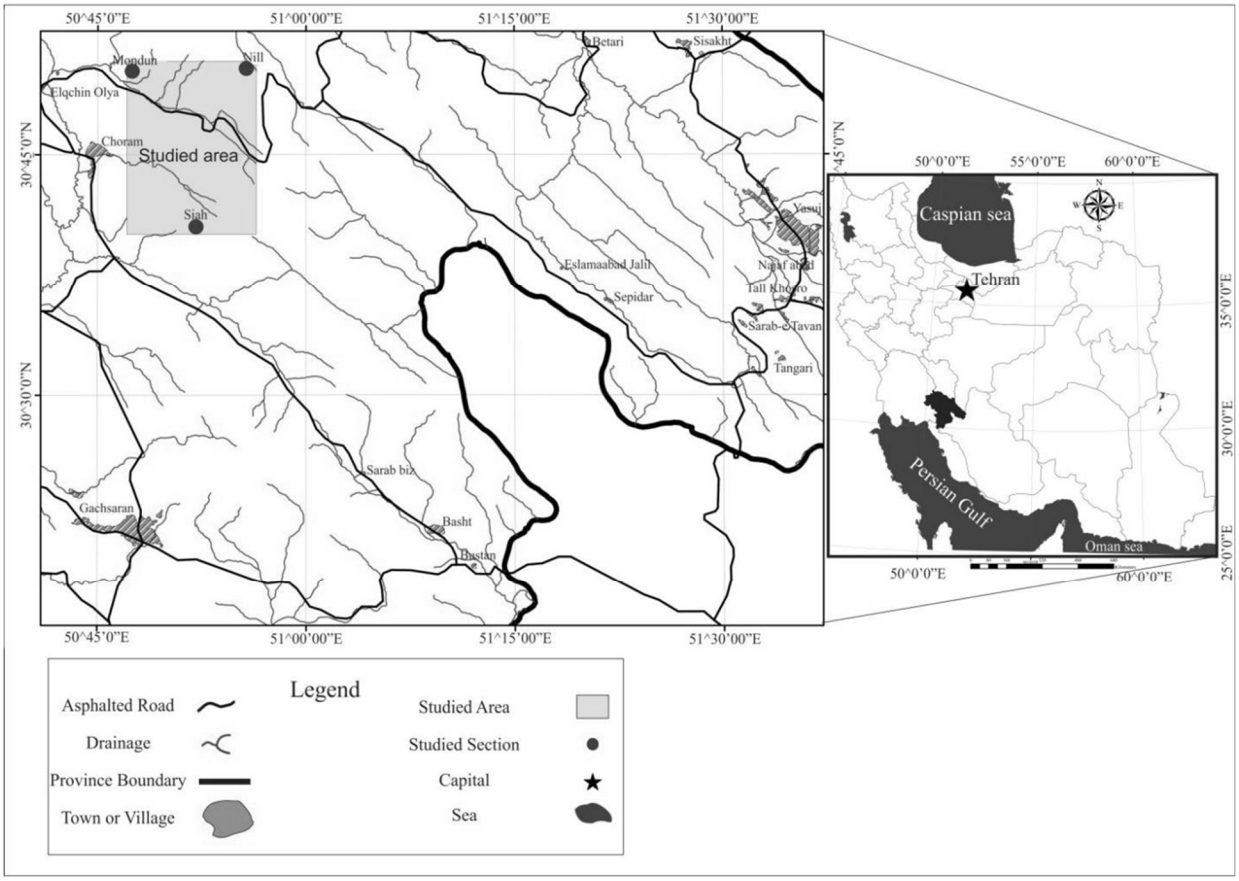

Figure 4. Regional and location maps showing the study area in the Zagros region (SW Iran).

2.1. The Nill section

The Nill Mountain is a well-developed anticline in which the Gurpi, Pabdeh and Asmari formations are exposed. The bottom of the section contains the upper part of the Gurpi Formation (6 m thick) that consists of thin to medium bedded grey marl interbedded with thin layers of argillaceous limestone. Results from petrographic studies of this formation show a dominance of pelagic facies with *Globotruncana* sp. (see Supplementary) The purple shale unit has not been exposed and alternating layers of dark grey shale and thin bedded limestone of the Pabdeh Formation unconformably overly the Gurpi Formation. Field evidences demonstrate that the Asmari Formation conformably overlies the Pabdeh Formation in this section. The base of the Asmari Formation shows alternating medium to thick bedded limestone and marl which gradually change to thick bedded limestone (Figure 5).

Figure 5. Field view of the upper boundary of the Pabdeh Formation in the Nill anticline showing alternating medium to thick bedded limestone and marl changing gradually to thick bedded limestone.

The Pabdeh Formation in Nill section composed of alternating bioturbated argillaceous limestone and black shales at the bottom. Rhythmic alternations between limestone, green marls and dark gray marls. The top of the Formation represents alternating marls and limestone horizons of varying thicknesses with abundant benthic foraminifera. Three phosphatic units developed within the Formation, separated by alternating dark grey shale and thin bedded limestones. The average total thickness of the phosphatic beds is 12 m. The first phosphatic horizon is dominated by phosphatized limestone with an average thickness of 6 m. The second phosphatic horizon consist of thin bedded limestone intercalated with phosphatized shale and marl with a total thickness of 2 m (Figure 6). The third phosphatic horizon is 4 m thick. The average grade of the phosphatic layers is 2.94% P_2O_5. Biostratigraphic studies of planktonic foraminifera and the presence of *Orbulinoides beckmani* (Supplimentary) indicate a Lutetian and Bartonian age for the second and third units respectively.

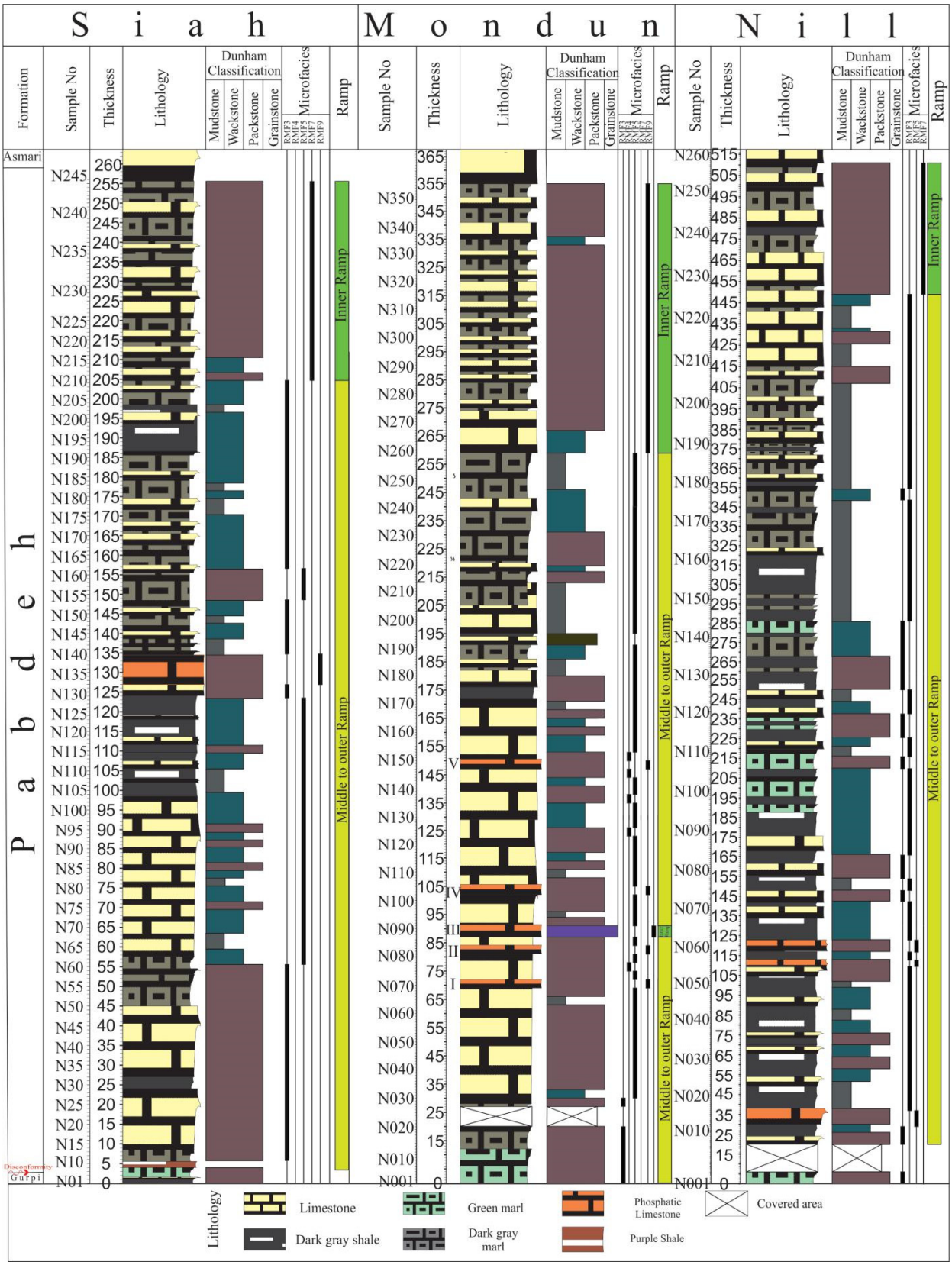

Figure 6. Stratigraphic and microfacies column of the Pabdeh Formation in the Nill, Mondun and Siah anticlines.

2.2. The Mondun section

The Mondun Anticline with a NW–SE trend is located 85 km north of Gachsaran. In this anticline the Pabdeh Formation (355 m) occurs on top of the Gurpi limestones with a distinct unconformity. The formation is divided into four stratigraphic units based on their sedimentological characteristics and fossil content (Figure 6). The purple shale unit at the base of the Pabdeh Formation has not been exposed in this outcrop, hence the lower part of the formation is greenish grey marl associated with thin interlayers of argillaceous cream limestone (25 m thick). Foraminiferal fauna indicates *Hantkenina nuttalli*, *Pseudohastigerina wilcoxensis*, *Dentoglobigerina yequaensis* and *Globigerinatheka index* (Supplimentary*)*. The second stratigraphic unit (120 m) is marked by thin to medium bedded limestone. The presence of planktonic foraminifera such as *Acarinina wilcoxensis*, *Acarinina collactea*, *Acarinina bullbrooki* and *Pesudohastigerina wilcoxensis* (Supplimentary) demonstrates that this horizon is of Early Eocene (Ypresian) age. The third stratigraphic unit (50 m thick) is characterized by alternating layers of dark grey shale, grey marls and thin bedded limestones. The forth part of the formation (135 m) is dominated by greenish grey shale with intercalation of thin to medium bedded beige to yellow pelagic limestone. This part is the uppermost part of the formation. Microfacies studies show well-rounded, well-sorted bioclastic, phosphatic, foraminiferal/oolitic grainstone (See section 4.3.1). All four horizons contain laminated and phosphatized-bedded bioclastic packstone.

The phosphatic horizons are present in five stratigraphic levels (from bottom to the top: layers I-V, Figure 6) separated by thin bedded planktonic foraminiferal-bearing limestones. All phosphatic horizons composed of phosphatized limestone. Their P concentration is commonly high (III and IV ~23% P_2O_5), and their carbonate content (mostly calcite) is generally high as well. The first and the second horizons (I and II) composed of alternations of phosphate-rich and carbonate-rich laminae.The P_2O_5 grade of these horizons are 5.51% and 5.08% respectively. The third phosphorite horizon consists of grainstone (1 m thick) facies with small phosphatized pellets, ooids, intraclasts and planktonic foraminiferal tests, fish scales and bones with the average grade of 25.12% P_2O_5. This is a well-sorted facies, in which the main allochems are dominantly superficial ooids and pellets (See section 4.3.1). Minor allochems are foraminiferal tests, fish scales and bones (Figure 7). The most distinctive feature of the third phosphatic layer (III) is the existence of ooid and pelletal phosphatized grains. The phosphate fraction of this horizon typically consists of medium-sized (>200 μm) phosphate grains, various amounts of phosphatized intraclasts, fish scales and bones. The common features of the fourth and fifth (V) phosphorite horizons is Shell-lag bedsand and the average grade are 22.32% and 4.12% respectively. The average total thickness of the phosphatic beds is 5 m.The Mondun phosphorite units are more lithologically and facially diverse than the others in the study area (See section 4.3.1). They are light brown, lithified, phosphatized pellet and oolite-rich and locally phosphatized granular beds, and exhibit distinctive high-grade mineralization in some levels. The average grade of the phosphatized layers in all horizons is 12.43% P_2O_5.

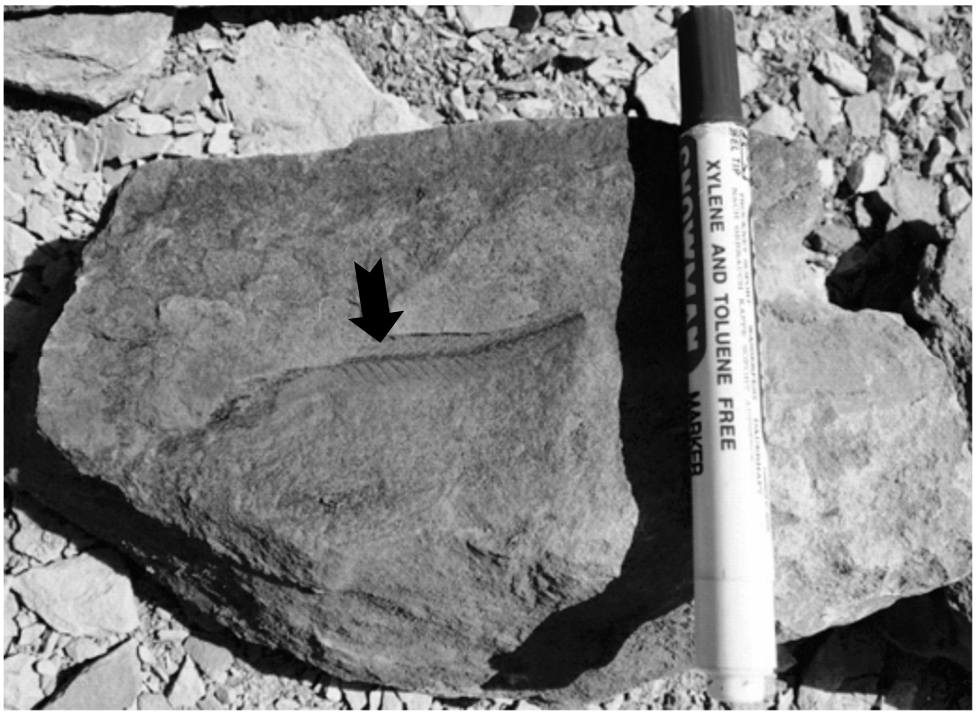

Figure 7. Field view from the Mondun section showing fish-scale in the third phosphorite unit.

2.3. The Siah section

The Pabdeh Formation on the north flank of the Siah anticline (60 km north of Gachsaran) is 255 m thick. The formation is divided into four stratigraphic units based on the sedimentological characteristics and fossil content (Figure 6).

The lower lithostratigraphical unit above the Gurpi Formation contains thin bedded purple shale (~2 m thick) which considered as a key layer of Pabdeh Formation in zagros region. The second stratigraphic unit (95 m thick) is marked by thin to medium bedded limestone. The third stratigraphic unit (98 m thick) is characterized by alternating layers of dark grey shale, grey marls and thin bedded limestone. The fourth unit of the formation (57 m thick) is dominated by greenish grey marl with intercalation of thin to medium bedded beige to yellow pelagic limestone. This is the uppermost part of the formation. The upper lithostratigraphic boundary with the Asmari Formation is transitional.

The phosphatic horizon (5 m thick), which is located 127 m from the bottom of the section (In the third stratigraphic unit), consists of phosphatized limestone. Field observations found sedimentological structures on these phosphatic horizons such as shell-lags, hummocky cross stratification and ripple marks on the top of the beds. The average grade of the phosphatic horizon is 5% P_2O_5.

3. Materials and method

Systematic sampling to examine the lithological variation was carried out in the sections. A total of 487 thin sections from the samples were prepared for petrographic studies (191 from the Nill, 170 from the Mondun and 126 from the Siah sections). The facies analysis was based on the petrographic

studies (microfacies description) and field observations (lithofacies description). The geometry of the sedimentary structures, the depositional textures, grain size, macrofaunal and trace fossil content, stratal surfaces and the stacking pattern of the facies were studied in the field. The microfossil content, lithology, depositional texture, and diagenesis were investigated in petrographic studies. We collected 37 samples from the phosphate horizons. Major and Trace element of whole rock analyses were analyzed at Kansaran Binaloud Co (Tehran, Iran). Major-elements [SiO_2, TiO_2, Al_2O_3, Fe_2O_3 (T), MnO, MgO, CaO, Na_2O, K_2O, P_2O_5] and selected trace elements (TEs: Ba, Sr, V, Y, Zr) determinations were obtained by Inductively Coupled Plasma - Atomic Emission Spectrometry (ICP-AES) analysis. Other TEs (Hf, Mo, Nb, Rb, Th, U) along with rare-earth elements (REEs): La, Ce, Pr, Nd, Sm, Eu, Gd, Tb, Dy, Ho, Er, Tm, Yb, Lu), were obtained by ICP-mass spectrometry (ICP-MS) analysis of the fusion solutions. Detection limits were 0.01% for all the major elements except MnO and TiO_2, for which the limits were 0.001%. The detection limits (ppm) for the TEs were: Sc, Th, U, 0.1; Hf, Sb, 0.2; As, Br, Cd, 0.5; Cu, Nb, Ni, Zn, 1; Mo, Rb, Sr, Y, 2; Ba, 3; Zr, 4; Cr, V, 5. The detection limits (ppm) for the REEs were: La, Ce, Nd, Sm, Gd, Tb, Dy, Ho, Er, Yb, 0.1; Pr, Eu, Tm, 0.05; Lu, 0.04. The XRD analysis was implemented at Kansaran Binaloud Co (Tehran, Iran).

Detailed palaeontological studies and biostratigraphic analysis of the samples were carried out using the biozonation model proposed by Wade et al. [58]. The microfacies classification of the carbonates was based on Dunham [59], Wilson [22] and Flugel [60].

4. Results

4.1. Petrography and mineralogy

Petrographical studies were performed using a Zeiss Axioplan 2 Polarized Light Microscope (Islamic Azad University,Science and Research branch, Tehran, Iran) and denote that calcite, quartz, pyrite and orthoclase are the gangue minerals. The Pabdeh Formation consist of a large variety of skeletal and non-skeletal grains, calcite cements and micrite. Differences in the abundance of allochems exist between the 3 study sections.

Non-skeletal grains are abundant in the Mondun anticline and consist mainly of ooids, intraclasts and peloids (Figure 8). The nuclei of ooids are commonly peloids, and in some cases the nuclei consist of the foraminiferal test. Intraclasts are present in all samples of the Nill, Mondun and Siah anticlines. Most intraclasts are consist of phosphate, while others contain bioclasts and peloids. Peloids are recognized in all sections, but are more abundant in Mondun anticline than in the Nill and Siah anticlines. In Phosphatized horizons of Mondun section, most pellets are uniform in size and have the small, similar-sized, well-sorted, uniform-shaped and orange colored. Skeletal grains are mostly, crinoids, bryozoas, ostracoda and plentiful planktonic and benthic foraminifera. Benthic Foraminifera such as *Heterolepa* sp, *Haplophragmium* sp., *Elphidium* sp., *Reusella* sp., *Nephrolepidina* sp., *Pseudolituonella reichelli* and *Pyrgo* sp and planktonic foraminifera such as *Acarinina* sp., *Morozovela* sp, *Globigerinatheka* sp, *Turborotalia* sp, *Hantkenina* sp., and *Globigerina* sp. (see Supplementary).

Intergranular space within the phosphatic and non-phosphatic grains display variable cementation by calcite (as a micrite, microsparite and rarely sparite). In phosphatized horizons these may also replace by the phosphatic grains. Petrographic studies shows similarities in the phosphatic constituents (pellets, phosphatized intraclasts, ooids, bioclasts including bone and teeth) of Pabdeh Formation in

comparison with the different deposits, but distinct variation in the non-phosphatic constituents (quartz, glauconite, lithoclasts, calcitic bioclasts and microcrystalline aggregates of carbonate minerals) was observed. Nonphosphatic constituents in the Pabdeh Formation phosphorites are dominated by calcite. Accessory minerals include glauconite and sulphides (pyrite) are present in some beds.

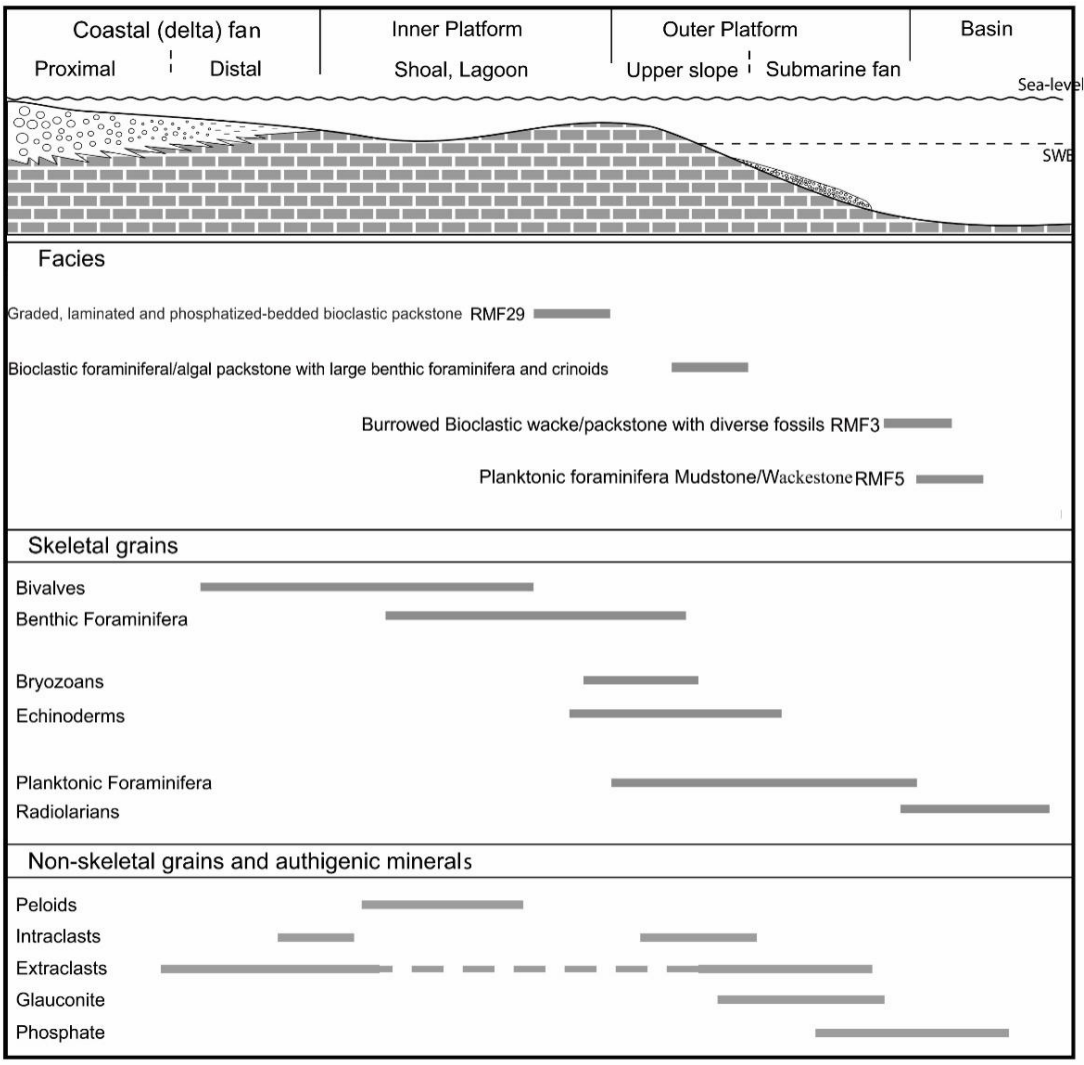

Figure 8. Schematic cross-section of depositional setting of Pabdeh Formation. Depositional environments, major energy levels, and lateral distributions of depositional facies and grain associations (skeletal and non- skeletal). Adapted from [61].

The results of the XRD analysis (Figure 9) demonstrate that the phosphatic ore minerals in the Pabdeh Formation are composed predominantly of fluorapatite while the associated gangue minerals include calcite, quartz, clay minerals (kaolinite, illite), pyrite and feldspars (orthoclase and albite).

The results of XRD analysis are presented in Table 1 and the results of major-element XRF analysis are presented in Table 2. Based on the tabulated results, it is evident that the phosphate deposits, with an initial P_2O_5 grade of 8–10%, are of a very low grade, and given the high CaO concentration, can be considered as sedimentary phosphate ore with carbonate gangue.

Table 1. X-ray diffraction (XRD) analysis of a representative phosphate ore sample from the Siah anticline.

Mineral type	Calcite	Quartz	Kaolinit	Illite	Fluorapatite	Other minerals	Total
%	67	6	5	2	18	2	100

Table 2. Major element geochemical analysis of a representative phosphate ore sample from the Siah anticline. L.O.I: Loss on Ignition.

Content	SiO_2	Al_2O_3	Fe_2O_3	CaO	Na_2O	K_2O	MgO	TiO_2	MnO	P_2O_5	S	L.O.I	Other	Total
%	9.24	2.45	1.67	46.01	0.28	0.38	0.72	0.102	0.012	9.164	0.003	28.98	0.989	100

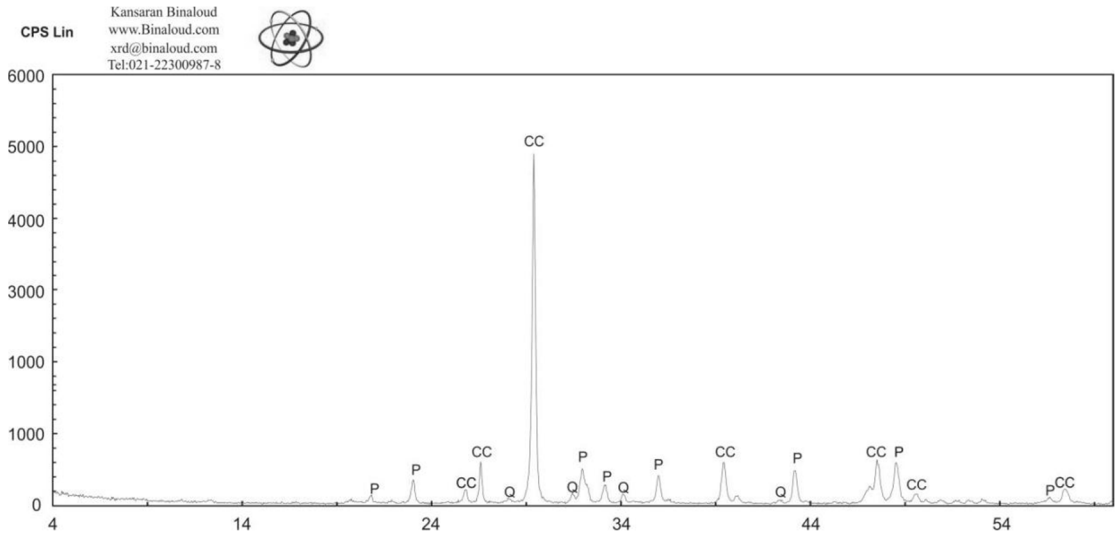

Figure 9. X-ray diffraction patterns Siah anticline phosphorite sample. P: apatite, CC: calcite, Q: quartz. Apatite and calcite are the major minerals.

4.2. Geochemistry

Phosphorites and its constituent apatite studied throughout the world for their economic importance [62] and especially the geochemistry of phosphorites is used to the estimation of paleo-marine geochemistry [63].

Phosphorites are generally contains considerable amount of trace elements and of REE and yttrium (Y) in respect to the average shale and other sedimentary rocks because of the substitution of REE^{3+} and Y^{3+} for Ca^{2+} in apatite [62,64–67]. The results of the major element, trace elements, and REY analyses for shales and phosphatic layers (Grey columns) obtained in the present study are presented in Table 3.

4.2.1. Major elements

The major oxides in the phosphate-bearing horizons are dominated by CaO, SiO_2 and P_2O_5, while Al_2O_3, Fe_2O_3 (T) are the next most abundant elements. The concentrations of all the other oxides [MgO, Na_2O, SO_3, MnO, K_2O, TiO_2] is generally low (<1%). The highest P_2O_5 values (20–25%) were

recorded in samples from the Mondun section (Table 3). Taking an average P_2O_5 content of 23% for fluorapatite yields an average fluorapatite content of 81% for the Mondun Basin sediments and 38% for the Siah and Nill Basins.

Samples from all three sections are characterized by the high CaO (32.45–48.65%) and very low MgO (0.4–1.09%) contents, reflecting high proportions of calcite and indicates that Mg might not have been incorporated in the apatite structure. The average concentration of CaO is about 40.43%. Weak correlation observed between CaO and P_2O_5 (R^2 = 0.014). The SiO_2 contents range from 6.37% to 31.35%, showing significant variation that reflects the changing proportion of quartz (detrital and from biogenic sources) [68]. The TiO_2 values vary between 0.004% and 0.19%, and are considered to represent mainly clay minerals as this element shows a relatively strong positive correlation with Al_2O_3 (R^2 = 0.47). The Al_2O_3 concentrations show significant variation (0.69–5.52%) that reflects the presence of clay mineral assemblages in the deposits. The alkali components Na_2O and K_2O show some variability (0.01% to 0.27% and 0.27% to 1.05%, respectively). Very weak correlation observed between Na_2O and P_2O_5 (R^2 = 0.019) and negative relationship between K_2O and P_2O_5 (R^2 = 053) may reflect Na and K substitution in the feldspar contents. The K_2O content is primarily determined by the type and amount of illite, glauconite and K-feldspar in the assemblage. The Fe_2O_3 contents range from 0.86% to 3.75%. The low values of Fe_2O_3 are due to the carbonate nature of mineralized and non-mineralized layers. The SO_3 content ranges from 0.002% to 0.41% which can be attributed to the occurrence of sulphate as a constituent element [67,69], and the presence of sulphides (pyrite) [70].

4.2.2. Trace elements

It is broadly recognized that an enriched trace elements group consisting Sc, Mo, Zn, Cd, Ag, U, Y, and REEs characterize the phosphorite facies [67,71–73].

The average concentrations of Trace Elements (ppm) in phosphatized samples in descending order is: Sr (1222.9 ppm), Cr (142.4 ppm), Ba (138.6 ppm), Zn (71.1 ppm), V (66.8 ppm), Ni (59.8 ppm), Cu (22.9 ppm), Mo (11.4 ppm), Zr (10.5 ppm), U (7 ppm), Th (6.8 ppm), As (6.6 ppm), Sc (4.5 ppm) and Sb (1 ppm). According to the elements concentrations, the distribution of trace elements in phosphorite horizons can be categorized into three groups: The first group composed of Cr and Ba, with relatively high concentrations (~140 ppm). The second group is made up TEs in moderate concentrations (10 to 70 ppm): Mo, Ni, Zn, V, Zr and CuThe third group consists of TEs in relatively low concentrations (<10 ppm): U, Th, Sc, As, and Sb.

Trace-element patterns

Compared with the Post Archean AustralianShale normalized (PAAS), there is major and traces elements fractionation (Figure 10a–c). For values >1, the concentrations of SiO_2, Al_2O_3, CaO, P_2O_5, Sr, Cd, Zn, Cr, Cu, Ni, Zr, Ba, Rb, Th, As and Sc are in excess relative to PAAS. If values are <1, the deficit is in relation to the composition of PAAS (Na_2O, TiO_2 and Fe_2O_3). MgO and Sb have values close to PAAS.

Strontium concentration in phosphorites of the study area varies from 486 to 2075 ppm. The good correlation between Sr and P_2O_5 (R^2 = 0.79) stated that Sr is situated in the fluorapatite structure. The relatively high concentration of Sr in these phosphorites may be due to the result of substitutes for Ca in fluorapatite [67]. Chromium content in these phosphorites ranges from 23 to 370 ppm with an average concentration of about 138.6 ppm. Positive correlation between Cr and P_2O_5 (R^2 = 0.81) reveals that Cr could be attributed in apatite structure.

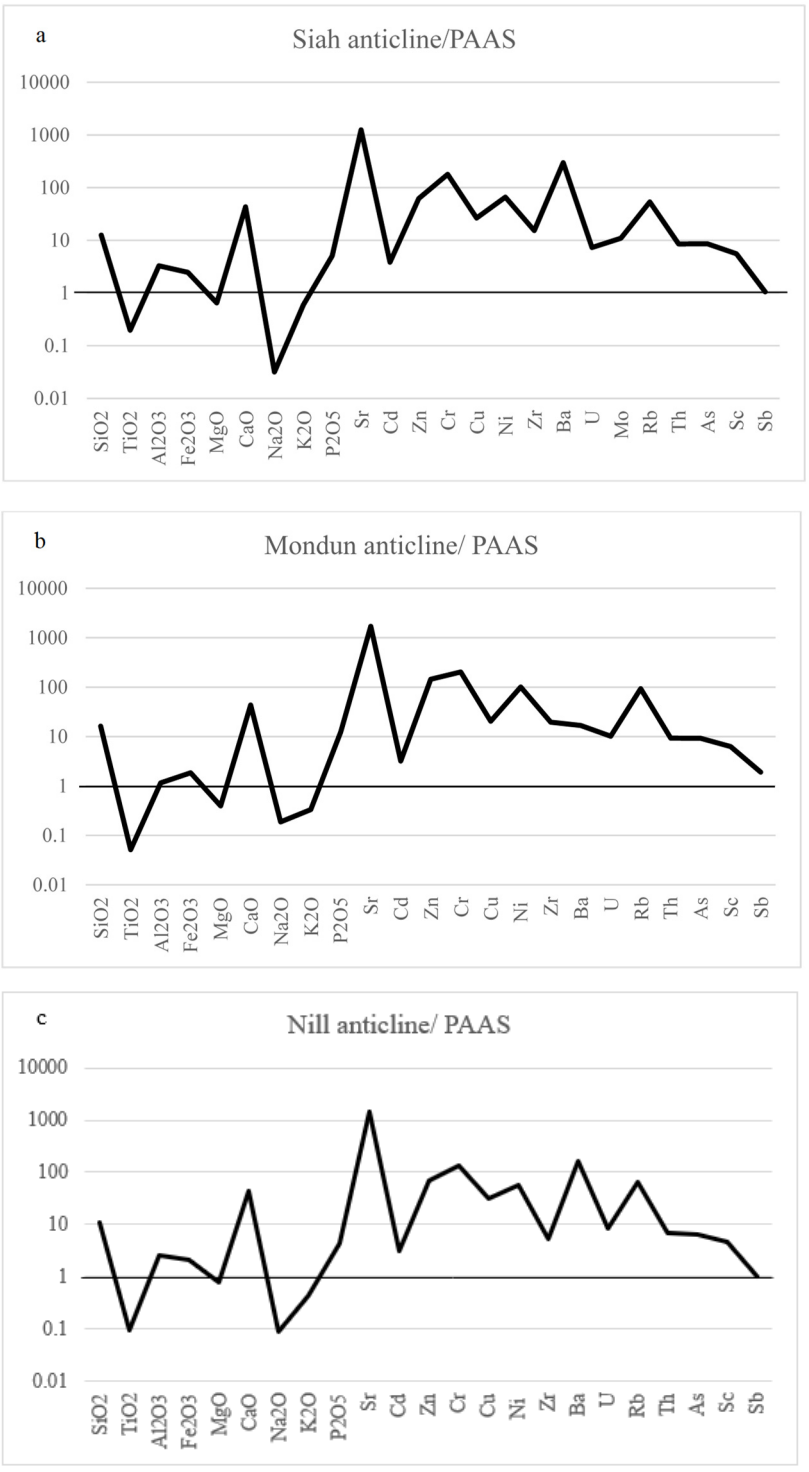

Figure 10. (a), (b), (c). Shale normalized (PAAS) averages major and trace elements spectra of phosphatic samples from Siah, Mondun and Nill sections.

Table 3a. Concentration of major elements (wt%), trace elements (ppm), rare earth elements (ppm), and elemental ratios in 14 phosphatic and non phosphatic samples from the Siah anticline.

Locality	Siah section							Phosphatic layers						
Sample No	N129	N130	N131	N132	N133	N134	N135	N136	N137	N138	N139	N140	N141	N142
Major Oxides%														
SiO_2	18.65	14.85	14.7	6.37	15.43	8.97	11.32	17	12.7	17.7	7.65	31	10.52	7.45
TiO_2	0.2	0.17	0.19	0.06	0.223	0.12	0.15	0.52	0.07	0.25	0.08	0.2	0.14	0.09
Al_2O_3	3.63	3.65	3.8	1.47	4.85	2.57	3.74	3.85	1.85	5.52	2.11	3	2.99	1.89
MnO	0.001	0.004	0.01	0	0.021	0.04	0.05	0	0	0.01	0	0	0.02	0.01
MgO	0.7	0.55	0.64	0.54	0.65	0.64	0.65	0.52	0.43	0.89	0.75	0.9	0.59	0.46
CaO	39.45	41.96	41.9	49.7	39.61	44.62	43.65	41.7	43.7	37.5	48.4	32	45.26	48.7
Na_2O	0.27	0.03	0.04	0.01	0.04	0.02	0.02	0.06	0.04	0.03	0.02	0.2	0.06	0.02
K_2O	0.81	0.68	0.78	0.31	0.77	0.55	0.7	0.62	0.37	1.05	0.29	0.6	0.54	0.35
P_2O_5	0.59	0.79	0.48	0.45	0.608	2.95	3.3	8.24	8.65	4.1	2.99	0.4	0.38	0.14
SO_3	0.002	0.013	0.06	0.03	0.012	0.06	0.1	0.36	0.12	0.2	0.01	0.3	0.03	0.01
L.O.I	33.02	33.66	34.9	39.6	32.33	36.67	33.14	24.2	28.7	29	36	28	37.6	39.7
Fe_2O_3	2.34	1.79	2.36	1.18	3.53	2.3	2.77	2.37	2.46	3.75	1.14	2.6	1.51	0.86
Total	99.663	98.15	99.7	99.6	98.07	99.51	99.59	99.4	99	100	99.4	100	99.64	99.6
TE (ppm)														
As	2.7	2.5	2.8	2	2.9	7.5	6.9	11.2	9.4	9.1	7.4	2.6	2.3	2.1
Ba	114	160	371	33	86	325	707	123	156	168	311	360	131	156
Cd	1	2.3	0.3	0.8	5	7.1	0.31	1.5	3.4	3.8	6.9	0.3	2.6	0.4
Cr	39	52	74	23	127	189	152	247	142	166	178	75	43	46
Cu	21	18	14	10	24	29	26	23	22	32	27	16	17	21
Mo	1.65	6.5	7.8	1.56	9.9	13.2	6	14	9.6	10.1	12.9	11	9.1	2.5
Ni	22	35	47	25	74	84	50	67	52	57	86	49	28	39
Sb	1.02	1.11	1.01	1.01	0.94	0.99	0.87	0.99	1.16	1.3	0.98	1	1.3	0.83
Sc	2.2	2.8	3.2	1.4	4.6	5.6	4.8	6.7	4.9	5.8	5.4	3.3	3.5	3.1
Sr	660	595	581	645	1032	1026	1060	1441	1325	1600	1033	592	486	536

Continued on next page

Locality	Siah section					Phosphatic layers								
Sample No	N129	N130	N131	N132	N133	N134	N135	N136	N137	N138	N139	N140	N141	N142
TE (ppm)														
Th	6.6	7.6	8.2	6.6	7.3	8.1	10.4	8.7	7.8	8.1	8.2	7.9	5.4	6.8
U	4.9	3.9	4.2	3.2	4.5	5.8	6.3	9.1	7.6	9.3	5.6	4.1	3.5	3.3
V	28	80	38	25	103	104	53	85	65	77	107	37	59	65
Rb	17	6	11	4	17	28	50	73	60	80	30	9	8	16
Zn	46	54	35	37	33	43	53	51	90	92	44	32	47	57
Zr	12	16	20	8	10	21	17	16	8	7	23	27	13	14
REE (PPM)														
La	8.53	9.2	4.8	7.73	6.5	17.72	22.43	31.1	33.2	26.7	20.2	6.6	4.42	4.59
Ce	17.14	11.4	7.17	14.3	7.36	23.09	30.49	37.2	37.5	32.3	26.7	7.1	6.29	6.7
Pr	2.08	2.14	1.78	1.58	1.1	2.19	2.82	5.21	5.24	3.01	1.98	1.5	0.96	0.99
Nd	5.32	6.21	3.5	4.3	4.1	19.07	24.77	28.7	29.1	25.4	21.7	4	3.22	3.01
Sm	1.32	0.92	0.73	1.29	0.71	1.11	1.28	4.04	4.3	1.99	2.09	1.6	0.59	0.51
Eu	0.39	0.22	0.18	0.25	0.15	0.28	0.49	0.97	0.99	0.65	0.42	0.2	0.12	0.1
Gd	1.42	0.91	0.61	1.21	0.68	1.21	2.37	4.62	4.98	2.51	3.06	0.7	0.57	0.47
Tb	0.17	0.22	0.15	0.13	0.15	0.21	0.41	0.87	0.93	0.5	0.37	0.1	0.13	0.14
Dy	0.93	1.14	0.64	0.93	0.82	2.22	3.2	5.61	5.86	3.49	2.87	0.8	0.72	0.53
Ho	0.26	0.29	0.2	0.19	0.19	0.41	0.9	1.29	1.4	0.91	0.69	0.2	0.15	0.13
Er	0.72	0.72	0.44	0.67	0.6	1.93	1.5	3.99	4.5	1.84	2.32	0.6	0.44	0.39
Tm	0.14	0.11	0.08	0.13	0.1	0.12	0.16	0.59	0.69	0.22	0.19	0.2	0.05	0.03
Yb	0.79	0.94	0.47	0.56	0.59	1.62	1.99	3.41	3.75	1.27	2.05	0.6	0.46	0.47
Lu	0.16	0.12	0.07	0.14	0.11	0.19	0.2	0.58	0.62	0.25	0.18	0.1	0.07	0.04
Y	6.96	9.96	6.67	6.4	7.65	37.87	52.48	59.9	61.1	52.3	45.6	7.2	5.99	4.73
∑REE	39.37	34.54	20.8	33.4	23.16	71.37	93.01	128	133	101	84.8	24	18.19	18.1
∑REE_Y	46.33	44.5	27.5	39.8	30.81	109.2	145.5	188	194	153	130	31	24.18	22.8
Ce/Ce*	1.065	0.627	0.733	0.956	0.6	0.565	0.587	0.547	0.529	0.543	0.577	0.559	0.714	0.714
La/Nd	1.603	1.481	1.37	1.8	1.585	0.929	0.906	1.08	1.14	1.05	0.93	1.7	1.373	1.52

Table 3b. Concentration of major elements (wt%), trace elements (ppm), rare earth elements (ppm), and elemental ratios in 14 phosphatic and non phosphatic samples from the Mondun anticline.

Locality	Mondun section													
Sample No	N69	N70	N71	N82	N83	N84	N88	N89	N90	N91	N92	N149	N150	N151
Major Oxides%														
SiO_2	13.83	16.51	16.38	15.88	19.38	13.78	14.38	11.85	14.56	16.64	14.54	13.62	19.17	14.54
TiO_2	0.035	0.052	0.01	0.036	0.08	0.079	0.024	0.036	0.026	0.033	0.004	0.041	0.063	0.004
Al_2O_3	1.66	1.13	2.37	3.1	1.6	1.64	1.88	0.69	0.95	2.62	1.82	1.61	1.41	1.98
MnO	0.007	0.002	0.003	0.006	0.001	0.063	0.004	0.001	0.002	0.0023	0.007	0.0055	0.001	0.0019
MgO	0.45	0.4	0.42	0.55	0.45	0.83	0.57	0.37	0.35	0.52	0.57	0.39	0.41	0.36
CaO	45.59	43.31	43.96	40.85	41.19	45.57	46.22	46.75	45.02	44.69	45.19	44.93	41.25	44.61
Na_2O	0.08	0.22	0.04	0.031	0.21	0.11	0.2	0.15	0.18	0.22	0.19	0.12	0.18	0.19
K_2O	0.33	0.28	0.45	0.72	0.36	0.27	0.51	0.38	0.34	0.47	0.41	0.41	0.3	0.41
P_2O_5	0.52	5.51	0.36	0.41	5.08	0.39	0.49	25.12	22.32	0.36	0.32	0.71	4.12	0.58
SO_3	0.29	0.06	0.43	0.02	0.12	0.09	0.35	0.22	0.27	0.23	0.16	0.25	0.03	0.18
L.O.I	34.29	30.47	33.4	35.71	29.02	35.06	33.52	11.93	13.97	32.49	33.95	35.44	30.89	34.57
Fe_2O_3	2.41	1.8	1.68	2.29	2.06	1.53	1.53	2.15	1.65	1.11	2.36	1.78	1.61	2.05
Total	99.492	99.74	99.5	99.6	99.551	99.412	99.68	99.647	99.638	99.385	99.52	99.307	99.434	99.476
TE (ppm)														
As	2.3	9.2	3.46	3.81	4.3	4.26	5.01	15.1	13.8	5.08	6.55	5.39	3.9	4.62
Ba	53	7	44	37	2	60	47	38	34	67	73	59	3	64
Cd	0.91	1.2	1.8	0.73	1.1	2.59	0.73	6.78	5.98	1.36	1.11	0.97	0.9	1.42
Cr	35	95	46	70	95	52	56	370	349	61.1	54	76	101	75.8
Cu	13	7	16	11	10	22	13	37	32	15	22	12	16	26
Mo	3.38	13.3	2.95	6.63	15.6	2.95	6.63	33	36	5.59	4.28	3.74	14.2	4.69
Ni	39	73	35	41	82	51	38	134	140	39	45	41	74	37
Sb	1.49	0.95	1.09	1.36	0.89	0.94	1.26	3.6	3.2	0.87	1.21	0.91	0.91	1.34
Sc	2.2	5.1	2.35	3.11	4.3	4.22	3.61	9.1	8.1	2.41	3.04	2.73	4.7	2.66
Sr	747	1503	690	587	1456	836	903	2075	1974	710	660	580	1499	690

Continued on next page

Locality	Mondun section													
Sample No	N69	N70	N71	N82	N83	N84	N88	N89	N90	N91	N92	N149	N150	N151
TE (ppm)														
Th	5.5	7.1	6.65	8.1	7.4	5.26	6.32	13.2	11.9	4.95	7.35	5.63	6.8	6.41
U	4.42	8.5	3.98	4.36	7.9	3.21	3.69	12.8	13.2	3.33	4.01	3.69	8.3	2.97
V	31	73	49	36	87	27	43	84	78	28	33	19	81	25
Rb	35	61	32	61	59	26	29	148	139	52	77	65	59	59
Zn	57	65	75	67	93	71	47	253	235	61	39	44	77	38
Zr	23	15	20	16	11	17	26	31	25	21	12	30	16	15
REE (ppm)														
La	6.77	26.79	6.85	8.25	24.61	9.94	14.3	32.4	28.4	8.54	10.2	7.91	22.88	8.02
Ce	11.9	34.02	11.3	7.97	33.26	6	10.6	59.5	50.24	5.7	9.93	7.12	34.26	4.97
Pr	2.14	4.33	1.55	2.35	5.02	2.3	4.52	7.76	6.03	2.69	2.36	2.73	4.18	1.92
Nd	5.39	15.38	3.9	4.46	17.77	7.58	7.48	21.8	20.01	2.87	3.58	3.01	16.57	3.02
Sm	1.05	4.53	0.79	0.73	4.61	0.75	1.02	5.49	4.86	0.43	0.81	0.56	4.19	0.55
Eu	0.61	0.99	0.21	0.16	1.13	0.11	0.51	1.23	0.93	0.12	0.36	0.16	1.05	0.14
Gd	1.2	7.1	1.31	0.72	6.86	0.75	1.27	7.41	6.43	0.53	2.36	0.58	6.92	0.67
Tb	0.17	0.78	0.15	0.15	0.91	0.22	0.27	0.99	0.9	0.09	0.34	0.1	0.83	0.1
Dy	0.89	5.41	0.81	0.93	5.95	1.17	1.15	6.58	5.72	0.48	2.01	0.6	4.88	0.55
Ho	0.24	1.22	0.19	0.25	1.37	0.32	0.32	1.67	1.24	0.18	0.54	0.15	1.11	0.26
Er	0.61	3.73	0.55	0.6	4.17	0.74	0.78	4.42	4.09	0.37	1.3	0.4	3.75	0.34
Tm	0.14	0.62	0.17	0.09	0.75	0.13	0.2	1.21	0.73	0.21	0.22	0.09	0.69	0.19
Yb	0.85	4.02	0.78	0.48	3.36	0.84	1.03	4.69	3.57	0.39	1.24	0.3	3.91	0.48
Lu	0.17	0.61	0.14	0.1	0.54	0.13	0.21	0.89	0.8	0.07	0.25	0.06	0.58	0.09
Y	8.44	57.7	7.99	8.63	60.48	11.2	9.12	73.6	66.9	4.56	14.38	5.53	56.34	5.04
∑REE	32.13	109.5	28.7	27.24	110.31	30.98	43.66	156.04	133.95	22.67	35.5	23.77	105.8	21.3
∑REE_Y	40.57	167.2	36.69	35.87	170.79	42.18	52.78	229.64	200.85	27.23	49.88	29.3	162.14	26.34
Ce/Ce*	0.850	0.670	0.885	0.493	0.672	0.284	0.408	0.93	0.876	0.3	0.173	0.24	0.75	0.363
La/Nd	1.25603	1.742	1.756	1.85	1.3849	1.3113	1.912	1.4862	1.4193	2.9756	2.849	2.6279	1.3808	2.6556

Table 3c. Concentration of major elements (wt%), trace elements (ppm), rare earth elements (ppm), and elemental ratios in 9 phosphatic and non phosphatic samples from the Nill anticline.

Locality	Nill Section								
Sample No	N12	N15	N18	N55	N56	N57	N58	N61	N63
Major Oxides%									
SiO_2	12.33	12.97	13.05	11.52	12.65	13.45	10.45	7.65	12.64
TiO_2	0.14	0.15	0.083	0.081	0.067	0.062	0.094	0.075	0.098
Al_2O_3	2.78	3.72	2.54	3.04	1.85	1.23	2.39	2.11	1.94
MnO	0.004	0.03	0.003	0.004	0.002	0.0032	0.015	0.001	0.005
MgO	0.67	1.09	0.71	0.61	0.43	0.58	0.88	0.75	0.64
CaO	42.31	42.68	44.02	42.26	43.68	42.97	44.78	48.37	43.54
Na_2O	0.06	0.2	0.07	0.04	0.04	0.14	0.06	0.02	0.087
K_2O	0.69	0.67	0.52	0.51	0.37	0.49	0.41	0.29	0.49
P_2O_5	0.3	2.01	0.32	0.62	8.65	0.53	0.62	1.98	0.36
SO_3	0.21	0.16	0.009	0.003	0.12	0.01	0.004	0.005	0.06
L.O.I	37.66	33.54	35.47	38.9	28.65	38.44	38.79	36.82	36.39
Fe_2O_3	2.04	2.63	2.55	1.71	2.46	1.41	1.09	1.14	2.95
Total	99.194	99.85	99.345	99.298	98.969	99.3152	99.583	99.211	99.2
TE (ppm)									
As	2.48	4.9	2.65	2.45	9.1	1.71	2.39	4.71	2.3
Ba	151.3	181	137	163	168	103	133	155	115
Cd	1.88	2.89	1.56	1.3	3.8	0.94	1.21	2.62	1.32
Cr	47.3	131	45.5	48.4	166	39.74	48.37	111	35.32
Cu	17.3	35	19.5	12	32	13	15.23	26	15.6
Mo	5.58	10.1	4.07	4.62	13.33	5.78	5.57	9.25	5.59
Ni	41.2	57	28.5	45	61	31	39.28	55	43
Sb	1.04	0.93	1.04	0.98	1.3	1.2	1.05	0.82	1.05
Sc	2.86	4.87	2.78	3.06	5.8	3.04	2.99	3.11	3.01
Sr	620	1507	612	607	1600	487	578	1321	562

Continued on next page

Locality	Nill Section								
Sample No	N12	N15	N18	N55	N56	N57	N58	N61	N63
TE (ppm)									
Th	7.27	6.44	7.4	6.9	8.1	5.23	6.93	6.13	6.6
U	4.16	8.71	4.02	3.96	9.3	3.16	3.88	6.54	3.79
V	42.35	77	48	53	83	35.67	43.54	62	44.23
Rb	9	59	11.3	10.2	80	8.2	9.88	50	9.6
Zn	41	77	35	45	92	51	41.66	44	43
Zr	13	5	12	9	7	15	11	4	13
REE (ppm)									
La	7.34	20.07	5.21	6.19	26.7	4.65	6.12	17.11	4.81
Ce	11.45	26.69	6.7	13.27	32.31	7.89	10.77	21.45	8.22
Pr	1.73	2.53	1.13	1.42	3.01	1.11	1.49	2.06	1.51
Nd	4.25	21.92	3.4	4.1	25.43	4.21	4.28	19.18	4.42
Sm	0.99	1.19	0.89	1.29	1.99	0.59	0.98	1.12	0.85
Eu	0.22	0.55	0.14	0.32	0.65	0.12	0.24	0.43	0.25
Gd	0.93	1.94	0.58	0.73	2.51	0.57	0.81	1.08	0.64
Tb	0.16	0.42	0.13	0.14	0.5	0.09	0.14	0.31	0.17
Dy	0.89	2.88	0.71	0.77	3.49	0.39	0.69	2.31	0.49
Ho	0.22	0.73	0.15	0.19	0.91	0.13	0.17	0.67	0.18
Er	0.66	1.72	0.49	0.52	1.84	0.32	0.51	1.7	0.37
Tm	0.1	0.17	0.08	0.13	0.22	0.05	0.09	0.13	0.04
Yb	0.51	1.8	0.47	0.43	1.27	0.4	0.49	1.17	0.39
Lu	0.12	0.19	0.07	0.05	0.25	0.08	0.1	0.13	0.14
Y	7.42	41.47	5.97	7.04	52.3	4.43	6.12	32.8	4.93
∑REE	29.57	82.8	20.15	33.41	101.08	20.6	26.88	68.85	22.48
∑REE_Y	36.99	124.27	26.12	39.81	153.38	25.03	33	101.65	27.41
Ce/Ce*	0.843	0.577	0.638	1.086	0.543	0.75	0.910	0.542	0.795
La/Nd	1.727059	0.9156	1.5324	1.7977	1.0499	1.10451	1.42991	0.8921	1.0882

Prevot and Lucas [74] reported that Cr is principally carried away by the apatite and is secure in clays so it can be stated that chromium concentration was secured in the clay and ironiferous minerals during the precipitation of phosphatic ores, thereby the relatively high concentration of Cr observed in phosphorites. Zn content in these phosphorites ranges from 23 to 253 ppm with an average concentration of 71.1 ppm. High concentration of Zn in Mondun phosphorites may be due to the availability of pyrite and plenty of organic matter. In these phosphorites, the Uranium occurs in small quantity which ranges from 2.97 to 13.2 ppm with an average concentration of 5.43 ppm (Table 3). This element is commonly believed to be easily incorporated into the apatite lattice [71,75,76]. Positive correlation between U and P_2O_5 ($R^2 = 0.77$) in this study, indicates that most of the uranium content held by the apatite phase in the phosphorites [71,77–82]. Zirconium expresses a weakpositive correlation with P_2O_5 ($R^2 = 0.086$) which indicates that Zr does not occur in apatite structure. Ni content in these phosphorites range from 22 to 140 ppm with an average 51.57 ppm. Positive correlation between Ni and P_2O_5 ($R^2 = 0.73$) suggest that a high amount of Ni may be located to the apatite lattice [83,84]. Individual phosphatic horizons from Mondun demonstrated the highest contents of Sr, Zn, Y, Ni and U, whereas phosphatic horizons from the Nill and Siah contained the highest Ba contents.

In the present investigation, Ba concentration ranges from 2 to 707. It can be mentioned that negative correlation of P_2O_5 with Ba suggest the limited substitution of Ca by Ba. Regardless of the fact that Ba and Sr have the same geochemical behavior because of the higher ionic radii, Ba cannot replace Ca in fluorapatite lattice as Sr [52]. An important possibility of higher concentration of Ba in Siah section may be due to the availability of barite occurrences in the depositional area [52].

Similar trends are not seen in the bulk non-phosphatic horizons (Table 3), although in this case individual Mondun non-phosphatic sediment samples exhibit very slight changes of TE concentrations.

The highest As and Sb concentrations occur in phosphorites from Mondun, attributable to the high glauconite content of the sediments [85,86]. Thorium contents range from 4.95 to 13.2 ppm. High Th values characterize the samples from the phosphorite beds of the Mondun section. This element can replace Ca in fluorapatite lattice because of their same ionic radii.

The cadmium concentrations in the Pabdeh phosphatic horizons are variable, particularly in some of the Siah section samples the cadmium content is 7.1 ppm (>1.1 average shale).

4.2.3. Rare-earth elements and yttrium

Rare earth elements used as a tools for identification of the depositional environmental system such as extensive marine anoxia [87–89], lithology and diagenesis [90–93], oceanic palaeo-redox conditions [94,95], and paleogeography and depositional models [96,97]. REEs are not easily fractionated at the time of sedimentation, and their patterns may provide a key to average provenance compositions [98]. Distribution pattern and concentration of REEs in phosphorites may be affected by weathering, burial diagenesis and metamorphic processes [99]. Recent studies of marine phosphorite deposits reveal that phosphorites can incorporate plenty of rare earth elements during their growth in oceanic sediments leading to very early diagenesis [100]. The enrichment of REEs in phosphorite layers have long been recognized for more than a century compared with other sedimentary rocks [101–103] because REE+Y are readily incorporated into the apatite structure directly from seawater during early diagenesis [67,99,104]. For example, fish debris apatite in slowly accumulating modern deep-sea muds may contain in excess of 3% ∑REE+Y [105].

Post-Archean Australian Shale normalized (PAAS) of Taylor & McLennan [106] selected to normalize the phosphorite REE in this study.

The REE+Y concentrations (ppm) and elemental ratios are presented in Table 3. The total REE (∑REE) and Y contents ranges from 27.1 to 103 and 7 to 52.2 ppm, respectively in average shale versus phosphorite horizons.

Samples from Mondun section (∑REE range 105.8 to 156.4 ppm, average 123.1 ppm) have higher REE contents than those from the Siah (84.8 to 133 ppm, average 101.9 ppm) and Nill (68.8 to 101 ppm, average 84.2 ppm) sections. These concentrations are comparable to the P_2O_5 contents in the Mondun samples. The Siah phosphate deposits (With the average of 84.2 ppm) is characterized by the lowest REE contents (Figure 11).

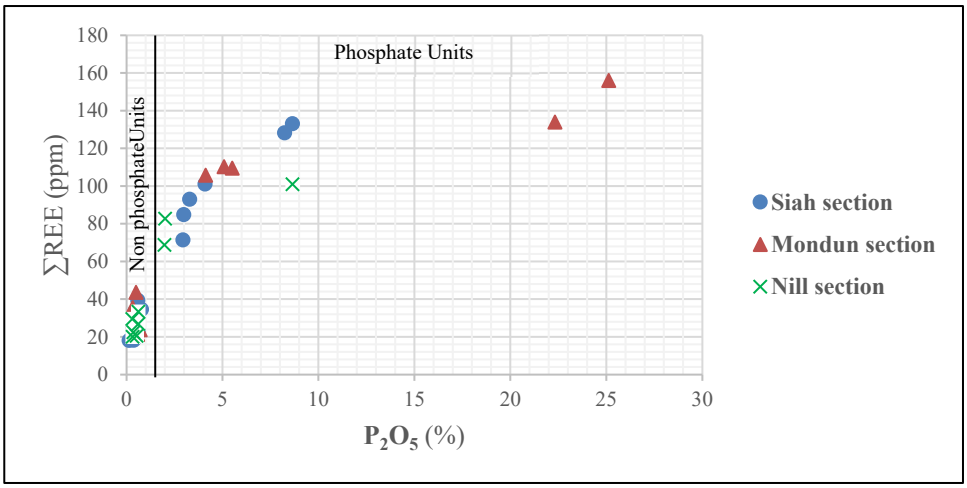

Figure 11. Bivariate plot of total rare-earth elements (∑REE, ppm) versus P_2O_5 (wt%) contents in Mondun, Nill and Siah phosphate and non-phosphate units.

It seems therefore that there is a competition between the REE into the apatite lattice. The shale normalized (PAAS) REE patterns (Figure 12c,d) of Mondun phosphorites are characterized by negative LREE (La, Ce, Pr, Nd) and enrichment in the middle REE (MREE) and Heavy REE (HREE). The lowest ∑REE concentrations, recorded at the Nill section, occur in low grade phosphate levels (P_2O_5 < 4.5%). Most phosphorite values in Nill and Siah sections are close to, or in some cases less than the PAAS (Figure 12a,b,e,f).

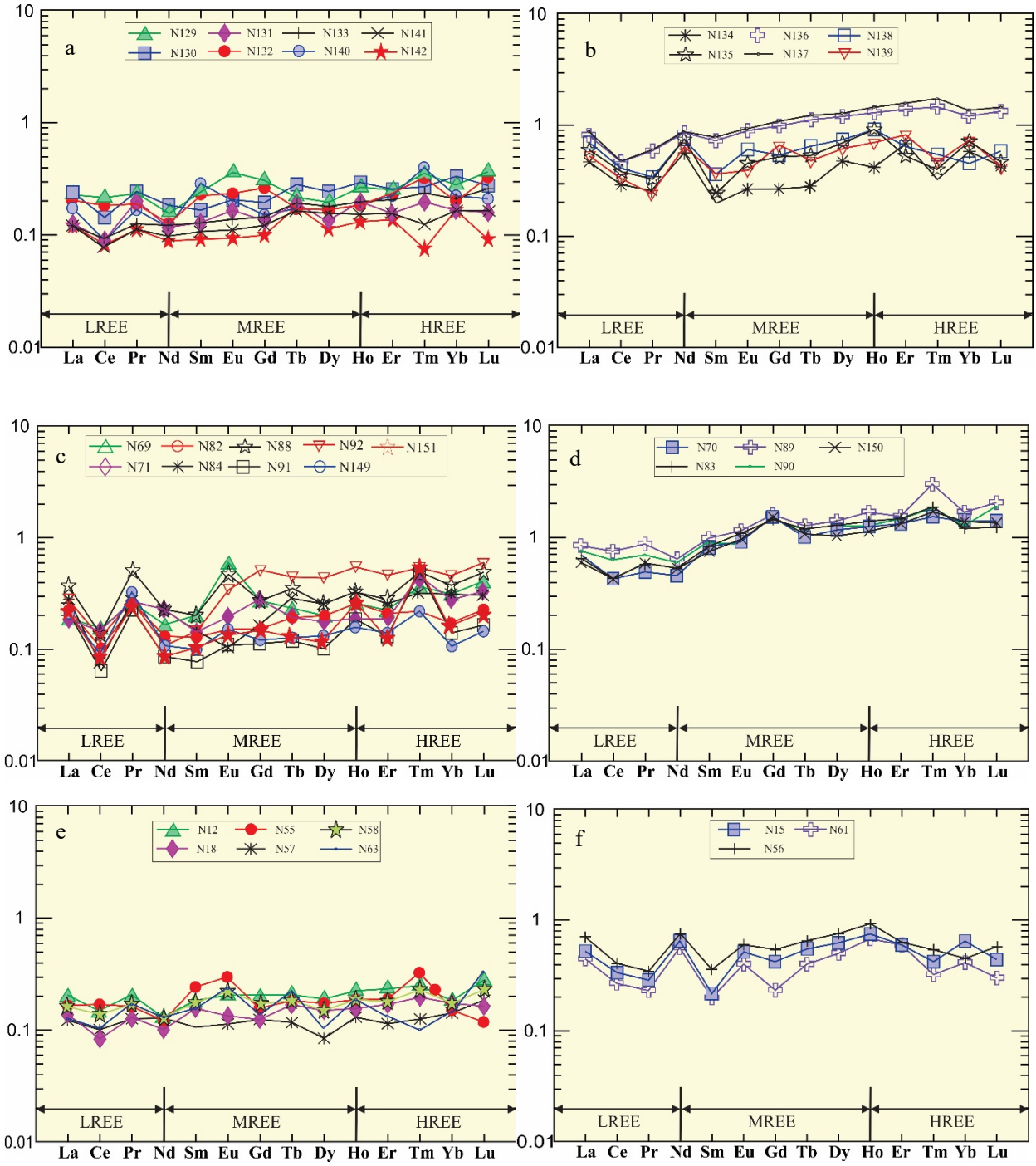

Figure 12. a, b, c, d, e, f. Rare earth elements normalized to PAAS (Post Archean Australian Shale, after Taylor and McLennan, [106] of non-phosphatized (a, c, e) and phosphatized (b, d, f) samples of Siah (a, b), Mondun (c, d), and Nill (e, f) sections.

Shale normalized REE patterns characteristically denote a progressive enrichment towards the heavier REE (HREE) and a relative depletion of cerium with respect to its REE neighbours lanthanum (La) and praesodymium (Pr) or neodymium (Nd). This negative Ce anomaly (Ce/Ce^{*}) is considered to relate to the decrease in solubility that accompanies the oxidation of Ce (III) to Ce (IV) and subsequent removal together with other multivalent metals [107].

The Ce anomaly (Ce/Ce^*) was applied by many authors [52,108–110]. The Ce anomaly calculated from:

$$[Ce^*=2/3La_N+1/3Nd_N;\ Ce/Ce^* = 3Ce_N/\ [2La_N+Nd_N] \quad (1)$$

where N refers to the Shale normalization of concentrations [88]. When Ce anomaly is equal to 1, indicate that there is no anomaly. For values lower than 1, it's described as negative and when it is higher than 1, described as positive [52].

Samples with negative Ce anomalies indicate that these phosphates have been formed in suboxic environments deficient in this element [107].

The REE pattern includes most of the phosphorite samples from all three sections, which have a strongly negative to positive Ce anomalies (values varying between 0.24 and 1.08). All the samples analysed present Shale normalized negative Ce anomalies of varying magnitudes. This anomaly, in addition to a HREE enrichment, is typical of ocean water REE composition [111].

Also there are strong positive correlations between ∑REE+Y and Ce anomaly in Mondun Section but conversely there are negative correlations between ∑REE+Y and Ce anomaly in Nill and Siah sections (Figure 13a–c) [67,99].

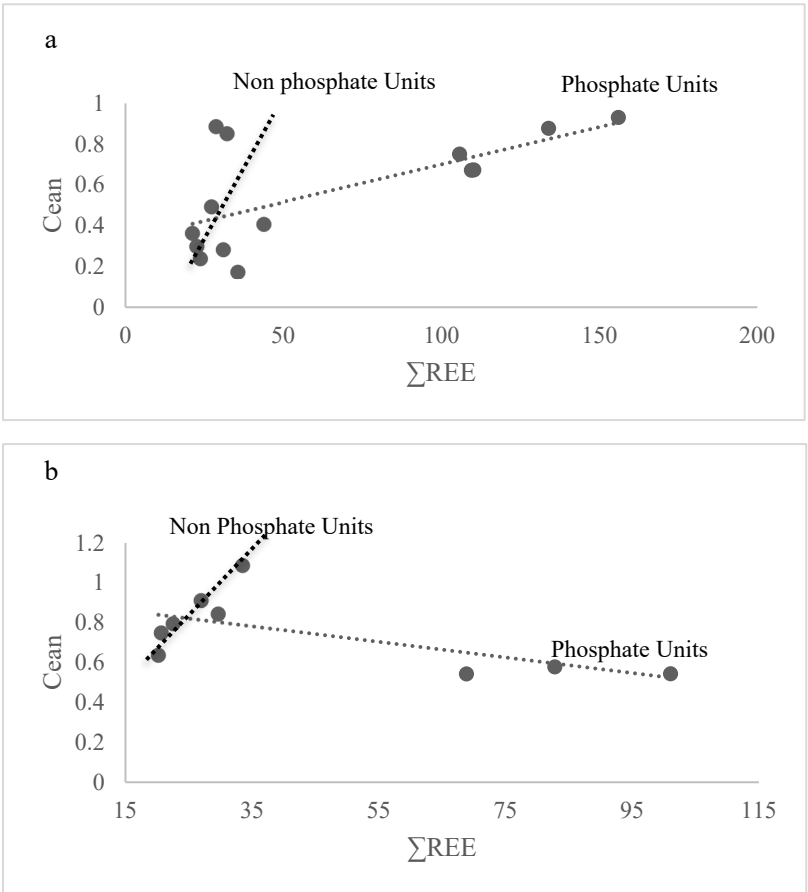

Figure 13. a, b, c. Ce_{an} versus ΣREE diagram of samples of Mondun (a), Siah (b) and Nill (c), profile showing positive correlation between the cerium anomaly values and the total REE in Mondun section and negative correlations in Siah and Nill sections.

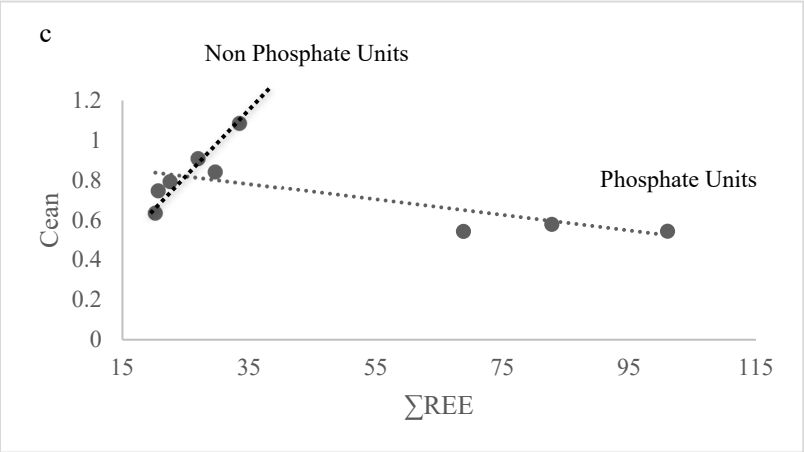

Figure 13. *Continued.*

4.3. Facies analysis

4.3.1. Carbonate facies

Based on field descriptions and petrographic studies, four sedimentary facies in addition to the basal purple shale and thin beds of marl with planktonic forams, such as Acarininidae, Globigerinidae, Morozovelidae, Turburotalidae Families and benthic forams, were identified in the Pabdeh Formation. Although previous studies identified pelagic shales of deep marine setting [3,112] we found shallow water carbonates and marls in the Pabdeh Formation samples. The carbonate facies are: (i) bioclastic mudstone/wackestone; (ii) burrowed bioclastic wackestone/packstone with diverse fossils; (iii) graded, laminated and phosphatized-bedded bioclastic packstone; and (iv) bioclastic foraminiferal/algal/peloidal packstone.

- **Bioclastic mudstone/wackestone**

This is a planktonic and benthic foraminiferal lime mudstone with intercalations of argillaceous limestone and marl. The constituent allochems of the facies are sparse planktonic foraminifera such as *Morozovellids*, *Hantkeninids*, *Pseudohastigerinids, Subbotinids*, *Turborotalids*, *Globigerinathekids*, *Orbulinids* and *Globigerinids* and benthic foraminifera such as *Elphidium* sp., *Heterolepa* sp. and scattered Echinoderms (Figure 14a,b).

Bioclastic mudstone/wackestonefacies occurs as limestone, dark grey shale and grey marls in the field. Low planktonic foraminiferal content and pyritization suggest that the bioclastic mudstone/wackestone microfacies were deposited below the Fair Weather Wave Base (FWWB), in a deep outer-ramp setting close to the basin edge.

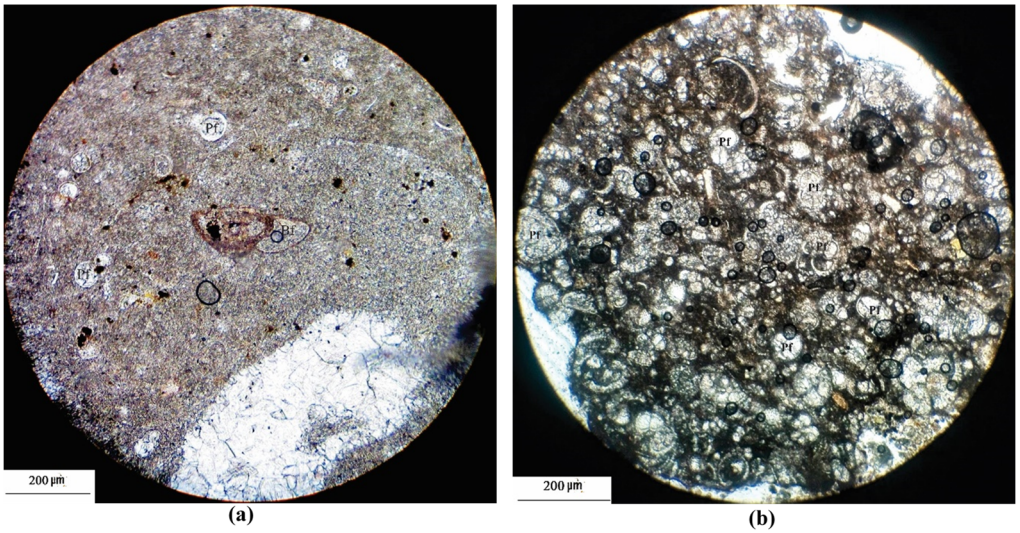

Figure 14. (a) Microphotograph of bioclastic mudstone to wackestone microfacies. Note the well-preserved benthic foraminifera. XPL; 200X. (b) Bioclastic pelagic foraminiferal packstone microfacies. XPL; 40X. Bf: Benthic Foraminifera, Pf: Planktonic Foraminifera.

- **Burrowed Bioclastic wacke/packstone with diverse fossils**

This is a bioclastic wacke/packstone with diverse fossils. The allochems consist of sparse fragments of planktonic and benthic foraminifera, echinoderm and echinoid spines and fragments. Horizontal and vertical burrows are common on the bedding planes (Figure 15a,b).

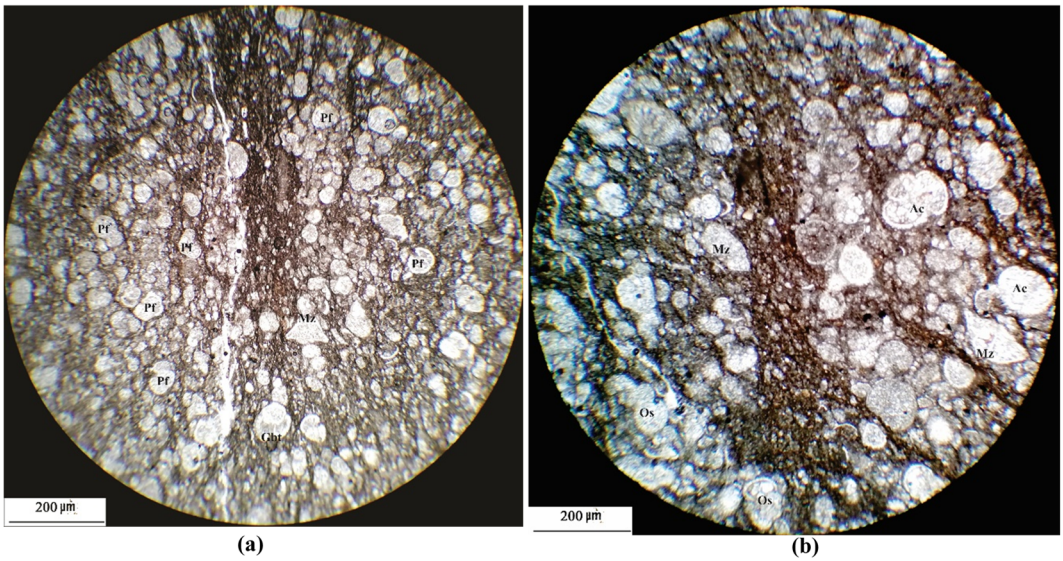

Figure 15. (a), (b). Microphotographs of burrowed bioclastic planktonic foraminiferal packstone showing shafts of vertical burrows formed in a deep marine environmental setting. Lower part of Pabdeh Formation. 200X; XPL. Note how the burrows are excavated to produce the micrite cavities. Bf: Benthic foraminifera; Pf: Planktonic foraminifera; Ac: Acarinina; Mz: Morozovella; Gbt: Globigerinatheka.

Burrowed Bioclastic wacke/packstone with diverse fossils were deposited below the FWWB in a deep outer-ramp setting close to the basin edge.

- **Graded, laminated and phosphatized-bedded bioclastic packstone**

The microfacies are characterized by interlayered dark mudstones and bioclastic packstone which has erosional basal contact, fining-upward succession and ripple marks on the top of the beds similar to Hips study [30]. Another characteristic feature of the microfacies is the occurrence of shell-lag beds which indicate deposition under episodic strong storm currents and various signs of reworking and transport of sediment from the inner ramp to this setting (Figure 16a). The bioclastic packstone consists of phosphatic ooids and phosphatized foraminifera, fossilized fish scales and bones and phosphatic intraclasts (Figure 16b,c).

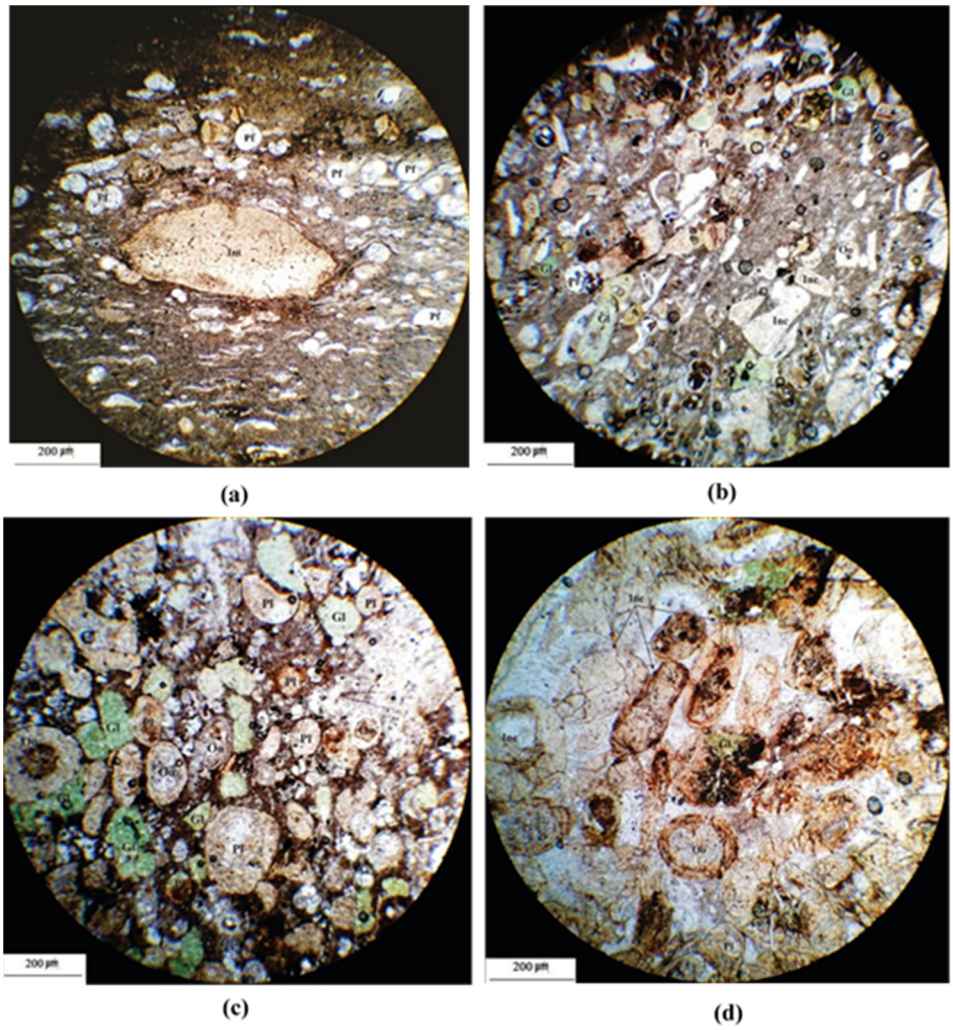

Figure 16. (a) Shell-lag beds in packstone microfacies. XPL; 200X. (b) Bioclastic, intraclastic, foraminiferal packstone with phosphatized foraminiferal tests. XPL; 40X. (c). Bioclastic, glauconitic, intraclastic and ooid packstone with fossilized fish scales, bones and small phosphatized foraminiferal tests. XPL; 200X. (d). Well-rounded, well-sorted bioclastic, oolitic, phosphatic, foraminiferal grainstone. Some phosphatic intraclasts and phosphatized foraminifera are also present. XPL; 200X. Bf: Benthic foraminifera; Pf: Planktonic foraminifera; Pl: Pellet; Oo: Ooid; Inc: Intraclast; Gl: Glauconite.

These microfacies occur in an outer ramp setting or near the middle–outer ramp boundary and are interpreted to have been deposited as carbonate tempestite, indicating storm influences on the ramp [17]. This microfacies is equivalent to the standard microfacies (SMF 14) of Wilson [22] and RMF 9 and RMF 29 of ramp carbonates [60]. Episodic strong storm currents transported sediment from the inner ramp to this setting. Well-rounded, well sorted bioclastic, phosphatic, foraminiferal oolitic grainstone (Figure 16d) is another characteristic feature of these microfacies, demonstrating deposition in a shallow-water setting which is equivalent to the RMF 29 of ramp carbonates [60].

The evidence for the origin of the storm in phosphatic Pabdeh Formation is the occurrences of packstone interbedded with bioturbated mudstones, commonly in upward fine grade form, ripple marks, and also hummocky cross stratification (HCS), which are also identified in field studies (Figure 17a,b). These features are good indicators of storm wave base (SWB) around 100 m, which is influenced by storm [113].

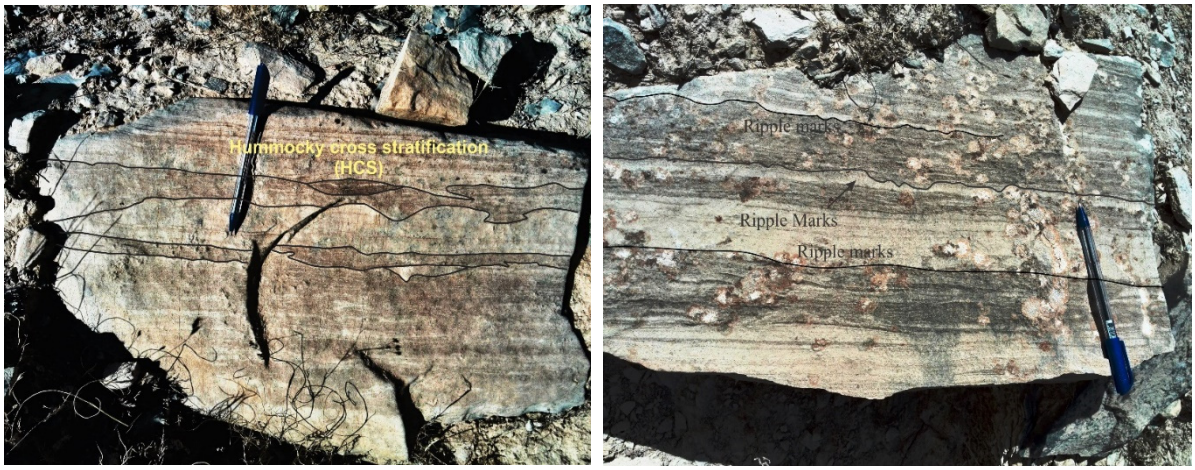

(a) **(b)**

Figure 17. (a) Field sample of phosphatized horizon from the Siah section showing hummocky cross stratification. (b) Ripple marks on top of phosphatic layers in the phosphatized horizon from the Siah section.

- **Bioclastic foraminiferal/algal packstone with large benthic foraminifera and crinoids**

This microfacies comprise the upper parts of the Pabdeh Formation with an overall thickness of about 164 m. They contain algae, benthic foraminifera (e.g. *Ditropa* sp., *Operculina* sp. (Supplementary), crinoids and bryozoans (e.g. *Tubucellaria* sp.). The planktonic foraminifera occur with low fossil content (Figure 18a,b). The main components of this microfacies are algae accompanied by benthic foraminifera. The upper boundary of these microfacies is graded and can be recognized by the first appearance of *Paragloburotalia kugleri* [114]. From a lithological point of view the contact with the overlying Asmari Formation is marked by a gradual change from the medium-bedded packstone of the Pabdeh Formation which contains thin particles of marls and limestone, to the massive bedded, cliff-forming limestone of the Asmari Formation, which contains large benthic foraminifera [17]. The first appearance of thick to massive bedded limestone identifies the boundary between the Pabdeh and Asmari formations.

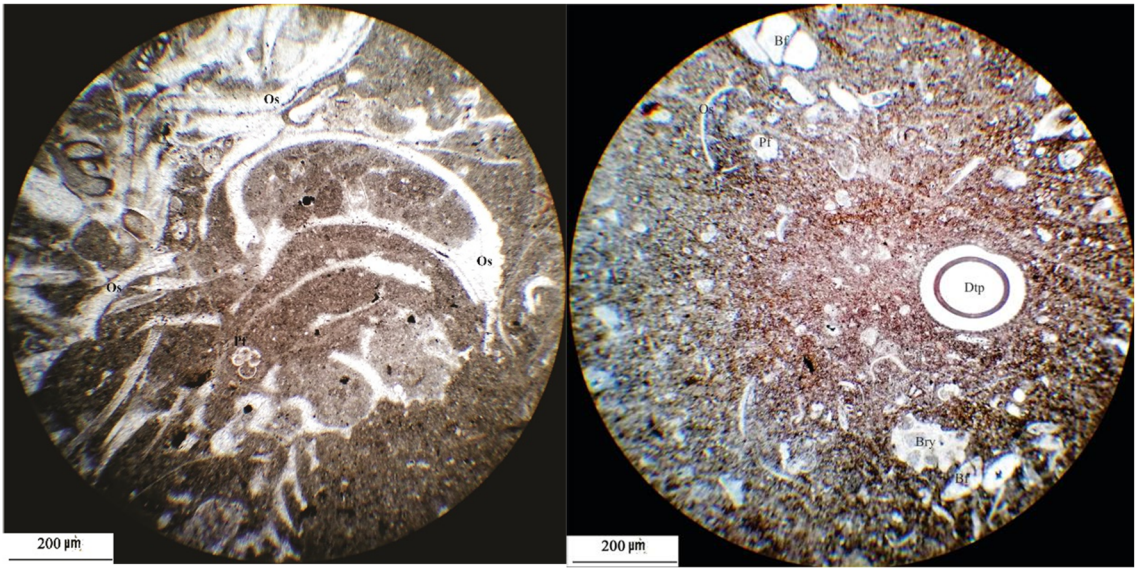

Figure 18. (a) Bioclastic foraminiferal algal packstone with large benthic foraminifera, ostracoda and bryozoan. (b) Bioclastic foraminiferal packstone with benthic foraminifera, bryozoan and ditropa. Dtp: Ditropa; Bry: Bryozoa; Bf: Benthic foraminifera; Pf: Planktonic foraminifera; Os: Ostracoda.

5. Discussion

Faunal association of Pabdeh Formation (including echinoderms, Benthic and Planktonic foraminifera, Bryozoan and Radiolaria) represents a foraminiferal-bryozoan association. These communities live in temperate and cold water and also at deeper settings in comparison to the tropical chlorozoan association [60,115].

The presence of sedimentological structures include of ripple marks, hummocky cross stratification (HCS), grainstone microfacies, the occurrence of bioclastic carbonates containing shallow water faunas in hemipelagic environments, burrows structures, shell lags, alternation of packstone and mudstone laminae which are also identified in field studies, indicate episodes of intense storm-generated currents activities. These storm currents carried carbonate sediments into the deeper parts of the basin, where they were deposited on top of mudstone with an erosional contact [17]. The findings of the depositional conditions of the facies indicate that the Pabdeh Formation was deposited on a carbonate ramp setting infuenced by repetition of storm conditions. The presence of algae and the abundance of benthic foraminifera (Nummulitidae family) in upper parts of Pabdeh Formation with no evidence of evaporative precipitation or restricted hypersaline microfauna suggest that this microfacies was deposited in the outer part of the Middle ramp setting or near the middle–outer ramp boundary and are interpreted to have been deposited as carbonate tempestite, indicating storm influences on the ramp [17].

Storm events significantly affected the phosphate deposition in the deep areas of the Pabdeh Formation while oceanic circulation, upwelling processes and cold nutrient-rich currents rising to the ocean surface were not involved in the formation of the phosphate horizons.

The lack of facies attributable to a rimmed shelf environment such as a shallow protected rimmed shelf with a shoal suggests that the depositional environment of the Pabdeh Formation was a distally steepened ramp. Storm currents in shallow areas provided well-rounded, well sorted foraminiferal oolitic grainstone from the back-shoal setting to the middle of the ramp. Other evidence for the ramp setting for the Pabdeh Formation includes the absence of either a slope break or abrupt facies changes from the platform to the deep basin [17].The lack of any marginal reef development, and the presence of pelagic microfauna and low-energy mudstone facies are evidence that the Pabdeh Formation was deposited on a carbonate ramp setting in this area.

Bioclastic mudstone/wackestone microfacies of Pabdeh Formation are comparable to the standard microfacies (SMF 3) of Wilson [22] and RMF 5 of ramp carbonates [60]. Burrowed Bioclastic wacke/packstone with diverse fossils of this formation are comparable to the standard microfacies (SMF 8) of Wilson [22] and RMF 3 of ramp carbonates [60].

Most of the sediments in the Pabdeh Formation were deposited in the middle and outer parts of the ramp. The distribution of these sediments in this setting was carried out by storm currents and turbidity systems.

The middle and outer ramp sediments comprise recurring facies which show alteration of mudstone and wacke to packstone laminations. Episodic storm currents transported sediments to these parts of the ramp forming a cyclic pattern of facies in the middle and outer ramp setting. Stratigraphically open marine outer-ramp pelagic facies gradually changed into middle-ramp facies influenced by marine currents. In the final stage of ramp development, a shallow carbonate shelf (the Asmari Formation) was deposited over the Pabdeh Formation as an overlying blanket [116,117]. Although strong agreement exists on the general character of the Pabdeh Formation, the palaeobathymetry of the pelagic deposits is still under debate. In this anticline, well-rounded, well sorted bioclastic, oolitic and phosphatic foraminiferal grainstone indicate shallow-water deposits from what were previously thought to be deep pelagic facies in the Pabdeh Formation. Shallowing-upward cycles, including some with prograding oolitic shoals at the top, appear again in these pelagic settings. Phosphatic grainstone formed through successive winnowing, transport and redeposition of phosphatic grains and intraclasts derived from shallow environments via storm-generated currents.

Trace element pattern indicate that Mondun section have the highest contents of Mo, Zn and Sb whereas phosphatic particles from the Nill section contained the highest amount of Ba, As, Cd, Cr, Cu, Ni, Sc, Sr, Th, V and Zr. Enriched concentration of Cu, Ni and Zn in the Nill phosphatic horizons has been considered to be typical of organic matter derived from marine plankton [118,119]. Copper and Ni provide the best proxies for organic carbon flux, itself a measure of surface-water productivity [120] andthe highest enrichment of Ba, As, Cd, Cr, Cu, Ni, Sc, Sr, Th, V and Zr in Nill and Siah sections is likely associated with low-grade P_2O_5 content.

Low iron contents in the Mondun phosphorites can be considered as a result of the presence of minor glauconite, ferromagnesian and pyrite minerals in the sediments. It's close to 2% Fe_2O_3 for all the sections. Although the highest P_2O_5 content occurs in the Mondun section, it also contains high amounts of Mo, Zn and Sb.

In contrast to the eastern Mediterranean and north and northwest Africa, where phosphate deposits formed in shallow marine depositional environments and evaporitic cycles, the phosphate horizons of Pabdeh Formation were formed in middle and outer ramp setting conditions. Several recent studies show evidence for depth control on the extent of Ce anomalies in marine authigenic minerals [94,121,122] where shallowing is associated with Ce depletion, Thus the Mondun section, with a reduced negative

cerium anomaly (0.56), represents highly reworked, bioturbated with higher energy realm conversely Nill section with Ce enrichment considered to represent deeper water sedimentation. REE data from the phosphatic horizons of Pabdeh Formation also supports the depositional conditions of the deep water environment for this nominated Formation. The Shale normalized REE patterns of Mondun phosphorites are characterized by negative Ce anomalies. This anomaly indicate that the depositional environment was oxic during phosphate deposition.

These geochemical findings are in accordance with microfacies studies which indicate shallow and high energy condition for Mondun section with negative cerium anomalies and a deep ramp setting for Nill and Siah sections which denote a positive cerium anomalies in REE patterns.

6. Conclusion

Major Eocene-Oligocene phosphate-bearing deposits occur in a ramp settings in south-western Iran: the Nill, Mondun and Siah basins.

The principal conclusions drawn from the study of these three sites are as follows.

Four lithofacies were identified at the three studied outcrop sections: (i) bioclastic mudstone/wackestone; (ii) burrowed bioclastic wacke/packstone with diverse fossils; (iii) graded, laminated and phosphatized-bedded bioclastic packstone; and (iv) bioclastic foraminiferal/algal/peloidal packstone.

Most of the carbonate sequences from the Pabdeh Formation were deposited in Middle to outer ramp environments in the Nill, Mondun and Siah anticlines.

Biostratigraphic studies of planktonic foraminifera and the presence of *Orbulinoides beckmani* (Supplementary) demonstrate that the first phosphatic horizon in all the sections is of middle Eocene age (Lutetian stage); the second and third horizons are Bartonian.

The Pabdeh Formation can be categorized in global terms as a low-grade ore deposit. The average grade of the Pabdeh Formation phosphate is 8–12% P_2O_5 but the average grade of phosphorites in Tethyan phosphate deposits is 25–30%.

Microfacies studies demonstrate that all the phosphatic ooids and phosphatized foraminifera, fish scales, bones and phosphatic intraclasts reworked from shallow parts of the Tethyan Ocean (in the eastern Mediterranean, north and northwest Africa e.g., Tunisia, Iraq, Saudi Arabia, Morocco and Algeria) to deeper parts with the help of turbidity currents. Storm-generated surges transported phosphate particles to the deeper inner ramp of the ocean where they were suspended and deposited alternately as shell-lag and phosphate laminations. This is the first report of phosphate-bearing horizons, previously thought to be formed in nutrient-rich currents, deposited in a deep-water environment. Major-element, TE and REE+Y data from the phosphorites demonstrate distinctive geochemical signatures in the three sections of the Pabdeh Formation. There are strong positive inter-elemental correlations between all the REE+Y and P_2O_5 which attest to their strong coherence as a geochemical group. The Mondun section, with a reduced negative cerium anomaly (0.56), represents highly reworked, bioturbated with higher energy realm conversely Nill section with Ce enrichment considered to represent deeper water sedimentation.

Acknowledgments

We thank Dalia Lahav-Jones, from Liwen Bianji, Edanz Group China (www.liwenbianji.cn/ac), for editing the English text of a draft of this manuscript and express appreciation to R&D department of Zarrin Industry and Mining Holding for their contribution to the quality of the scientific results by proving us with pertinent invaluable data. We would also like to express our deepest gratitude to the Earth sciences Faculty of Islamic Azad University Science & Research branch for giving us access to their laboratory equipment.

Conflict of interest

The authors declare no conflict of interest in publishing this article.

References

1. Versfelt Jr PL (2001) Major Hydrocarbon potential in Iran, In: Downey MW, Threet JC, Morgan WA, *Petroleum provinces of the twenty first century*, American Association of Petroleum Geologists Memorial, 74: 417–427.
2. Alavi M (2004) Regional stratigraphy of the Zagros fold-thrust belt of Iran and its proforeland evolution. *Am J Sci* 304: 1–20.
3. James GA, Wynd JG (1965) Stratigraphic Nomenclature of Iranian Oil Consortium Agreement Area. *AAPG Bull* 49: 2182–2245.
4. Ala MA, Kinghorn RRF, Rahman M (1980) Organic geochemistry and source rock characteristics of the Zagros petroleum province: South West Iran. *J Pet Geol* 3: 6l–89.
5. Bordenave ML, Bunwood R (1990) Source rock distribution and maturation in the Zagros orogenic belt-provenance of the Asmari and Bangestan reservoir oil accumulations. *Org Geochem* 16: 369–378.
6. Bordenave ML, Huc AY (1995) The Cretaceous source rocks in the Zagros Foothills of Iran. *Rev Inst Fr Pet* 50: 721–752.
7. Daraei M, Amini A, Ansari M (2015) Facies analysis and depositional environment study of the mixed carbonate–evaporite Asmari Formation (Oligo-Miocene) in the sequence stratigraphic framework, NW Zagros, Iran. *Carbonates Evaporites* 30: 253–272.
8. Berberian M, King GCP (1981) Towards a paleogeography and tectonic evolution of Iran. *Can J Earth Sci* 18: 210–265.
9. Lees GM, Falcon NL (1952) The geographical history of the Mesopotamian plains. *Geogr J* 118: 24–39.
10. Purser BH (1973) Sedimentation around bathymetric highs in the southern Persian Gulf, In: Purser BH, *The Persian Gulf: Holocene carbonate sedimentation and diagenesis in a shallow epicontinental sea*, Berlin and New York: Springer-Verlag, 157–177.
11. Kassler P (1973) The structural and geomorphic evolution of the Persian Gulf, In: PurserBH, *The Persian Gulf: Holocene carbonate sedimentation and diagenesis in a shallow epicontinental sea*, Berlin and New York: Springer-Verlag, 11–32.
12. Baltzer F, Purser BH (1990) Modern alluvial fan and deltaic sedimentation in a foreland Tectonic setting: the lower Mesopotamian plain and the Arabian Gulf. *Sediment Geol* 67: 175–195.

13. Stocklin JA (1974) Northern Iran: Alborz Mountains, Mesozoic–Cenozoic orogenic Belt, data for orogenic studies. *Geological Society of London Special Publication*, 4: 213–234.
14. Takin M (1972) Iranian geology and continental drift in the Middle East. *Nature* 235: 147–150.
15. Alavi M (2007) Structures of the Zagros fold-thrust belt in Iran. *Am J Sci* 307: 1064–1095.
16. Sharland PR, Archer DM, Casey RB, et al. (2001) Arabian plate sequence stratigraphy. Gulf Petro link: Manama, Bahrain, 371–384.
17. Mohseni H, Al-Aasm IS (2004) Tempestite deposits on the storm influenced carbonate ramp: An example from the Pabdeh Formation (Paleogene), Zagros basin, SW Iran. *J Pet Geol* 27: 163–178.
18. Mohseni H, Behbahani R, Khodabakhsh S, et al. (2011) Depositional environments and trace fossil assemblages in the Pabdeh Formation (Paleogene). Zagros Basin, Iran. *Neues Jahrb Geol Paläontol* 262: 59–77.
19. Bolourchifard F, Fayazi F, Mehrabi B, et al. (2019) Evidence of high-energy storm and shallow water facies in Pabdeh sedimentary phosphate deposit, Kuhe-Lar-anticline, SW Iran. *Carbonate Evaporite* 34: 1703–1721.
20. Bahrami M (2009) Microfacies and Sedimentary Environments of Gurpi and Pabdeh Formations in Southwest of Iran. *Am J Appl Sci* 6: 1295–1300.
21. Rezaee P, Nejad SAA (2014) Depositional evolution and sediment facies pattern of the tertiary basin in southern Zagros, South Iran. *Asian J Earth Sci* 7: 27–39.
22. Wilson JL (1975) *Carbonate Facies in Geologic History*. Berlin, Germany: Springer-Verlag, 471.
23. Carozzi AV, Gerber MS (1978) Sedimentary Chert Breccia: A Mississippian Tempestite. *J Sediment Pet* 48: 705–708.
24. Bourgeois JA (1980) Transgressive Shelf Sequence Exhibiting Hummocky Stratification: The Cape Sebastian Sandstone (Upper Cretaceous), Southwestern Oregon. *J Sediment Pet* 50: 681–702.
25. Kreisa RD (1981) Storm-Generated Sedimentary Structures in Subtidal Marine with Examples from the Middle and Upper Ordovician of Southwestern Virginia. *J Sediment Pet* 51: 823–848.
26. Walker RG (1984) General Introduction: facies, facies sequences and facies models, In: Walker RG, *Facies Models*, Canada: Geoscience, 1–9.
27. Vera JA, Molina JM (1998) Shallowing-upward cycles in pelagic troughs. (Upper Jurassic, Subbetic, Southern Spain). *Sediment Geol* 119: 103–121.
28. Cheel RJ, Leckie DA (1993) Coarse grained storm beds of the upper Cretaceous Chungo Member (Wapiabi Formation), Southern Alberta, Canadian. *J Sediment Pet* 62: 933–945.
29. Molina JM, Ruiz-Ortiz PA, Vera JA (1997) Calcareous tempestites in pelagic facies (Jurassic, Betic Cordilleras, Southern Spain). *J Sediment Pet* 109: 95–109.
30. Hips K (1998) Lower Triassic storm-dominated ramp sequence in northern Hungary: an example of evolution from homoclinal through distally steepened ramp to Middle Triassic flat-toped platform, In: Wright V, Burchette TP, *Carbonate Ramps*, London: Geological Society of London, Special Publication, 149: 315–338.
31. Abed AM (2013) The eastern Mediterranean phosphorite giants: An interplay between tectonics and upwelling. *GeoArabia* 18: 67–94.
32. Jasinski SM (2003) Phosphate rock. United States Geological Survey Minerals Yearbook, 56.1–56.5.

33. Jasinski SM (2011) Phosphate rock. *Mineral Commodity Summaries 2011*, United States Geological Survey, United States Government Printing Office, Washington, D.C.
34. Van Kauwenbergh SJ (2010) World phosphate rock reserves and resources. International Fertilizer Development Center (IFDC), Technical Bulletin no. 75, Muscle Shoals, Alabama, USA, 58.
35. Lucas J, Prévôt L (1975) Les marges continentales, pièges géochimiques, l'example de la marge atlantique de l'Afrique a la limite Crétacé-Tertiaire. *Bull Soc Géol Fr* 7: 496–501.
36. Notholt AJG (1980) Economic phosphatic sediments-mode of occurrence and stratigraphical distribution. *J Geol Soc Lond* 137: 793–805.
37. Lucas J, Prévôt L (1995) Tethyan phosphates and bioproductites, In: Nairn AEM, Stehli FG, *The Ocean Basins and Margins—The Tethys Ocean*, Plenum Press, 8: 367–391.
38. Follmi KB (1996) The phosphorus cycle, phosphogenesis and marine phosphate-rich deposits. *Earth-Sci Rev* 40: 55–124.
39. Soudry D, Glenn CR, Nathan Y, et al. (2006) Evolution of the Tethyan phosphogenesis along the northern edges of the Arabian-African shield during the Cretaceous–Eocene as deduced from temporal variations in Ca and Nd isotopes and rates of P accumulation. *Earth-Sci Rev* 78: 27–57.
40. Al-Bassam KS (1989) The Akashat phosphate deposits, Iraq. In: NothoIt AJG, Sheldon RP, Davison DF, *Phosphate Deposit of the World, Phosphate Rock Resources*, Cambridge Univ. Press, 2: 316–322.
41. Jones RW, Racey A (1994) Cenozoic stratigraphy of the Arabian Peninsula and Gulf. In: Simmons MD, *Micropalaeontology and Hydrocarbon Exploration in the Middle East*. London, Chapman and Hall, 273-307.
42. Bramkamp RA (1941) Unpublished report, In: Cavelier C, *Geological description of the Qatar Peninsula*, Qatar, Bureau de recherches géologiques et minières, 39.
43. Soudry D, Nathan Y, Ehrlich S (2013) Geochemical diagenetic trends during phosphorite formation-economic implications: The case of the Negev Campanian phosphorites, Southern. *Sedimentology* 60: 800–819.
44. Follmi KB, Garrison RE (1991) Phosphatic sediments, ordinary or extraordinary deposits? The example of the Miocene Monterey Formation (California), In: Muller DW, McKenzie JA, Weissert H, *Geologic Events and Non-Uniform Sedimentation*, London, Academic Press, 55–84.
45. Zaïer A, Beji-Sassi A, Sassi S, et al. (1998) Basin evolution and deposition during the Early Paleocene in Tunisia. In: Macgregor DS, Moody RTJ, ClarkLowes DD, *Petroleum Geology of North Africa*, London, Geological Society of London Special Publication, 132: 375–393.
46. Burollet PF (1956) Contribution à l'étude stratigraphique de la Tunisie Centrale. *Ann Mines Géol* 18: 352.
47. Fournier D (1978) Nomenclature lithostratigraphique des série du Crétacé supérieur au Tertiaire de Tunisie. *Bull Cent Rech Explor Prod Elf-Aquitaine* 2: 97–148.
48. Sassi S (1974) La sédimentation phosphatée au Paléocène dans le Sud et le Centre Ouest de la Tunisie. Thesis Doctorat. d'Etat ès-Sciences, Université de Paris-Orsay, France, 300.
49. Chaabani F (1995) Dynamique de la partie orientale du bassin de Gafsa au Crétacé ET au Paléogène: Etude minéralogique ET géochimique de la série phosphate Eocène, Tunisie méridionale. Thèse Doc. Etat, Univ. Tunis II. Tunisie.

50. Henchiri M, Slim-S'Himi N (2006) Silicification of sulfate evaporites and their carbonate replacement in Eocene marine sediments, Tunisia, two diagenetic trends. *Sedimentology* 53: 1135–1159.
51. Chaabani F, Ounis A (2008) Sequence stratigraphy and depositional environment of phosphorite deposits evolution: case of the Gafsa basin, Tunisia. Conference abstract at the Intern. Geol. Cong. Oslo.
52. Galfati I, Sassi AB, Zaier A, et al. (2010) Geochemistry and mineralogy of Paleocene–Eocene Oum El Khecheb phosphorites (Gafsa-Metlaoui Basin) Tunisia. *Geochem J* 44: 189–210.
53. Kocsis L, Gheerbrant E, Mouflih M, et al. (2014) Comprehensive stable isotope investigation of marine biogenic apatite from the late Cretaceous-early Eocene phosphate series of Morocco. *Palaeogeogr Palaeoclimatol Palaeoecol* 394: 74–88.
54. Messadi AM, Mardassi B, Ouali JA, et al. (2016) Sedimentology, diagenesis, clay mineralogy and sequential analysis model of Upper Paleocene evaporitecarbonate ramp succession from Tamerza area (Gafsa Basin: Southern Tunisia). *J Afr Earth Sci* 118: 205–230.
55. El-Naggar ZR, Saif SI, Abdennabi A (1982) Stratigraphical analysis of the phosphate deposits in Northwestern Saudi Arabia. Progress report 1–4 submitted to SANCST, Riyadh. Saudi Arabia.
56. Baioumy H, Tada R (2005) Origin of Late Cretaceous phosphorites in Egypt. *Cretaceous Res* 26: 261–275.
57. Scotese CR (2014) The PALEOMAP Project Paleo Atlas for ArcGIS, version 2, Volume 1, Cenozoic Plate Tectonic, Paleogeographic, and Paleoclimatic Reconstructions, PALEOMAP Project, Evanston, IL, Maps 1–15.
58. Wade BS, Pearson PN, Berggren, WA, et al. (2011) Review and revision of Cenozoic tropical planktonic foraminiferal biostratigraphy and calibration to the geomagnetic polarity and astronomical time scale. *Earth-Sci Rev* 104: 111–142.
59. Dunham RJ (1962) Classifications of carbonate rocks according to depositional texture. In: Ham WE, *Classification of Carbonate Rocks—A Symposium*, AAPG Special Publications, 108–121.
60. Flugel E (2010) *Microfacies of Carbonate Rocks, Analysis, Interpretation and Application*, 2nd Edition. Berlin: Springer-Verlag, 984.
61. Omidvar M, Safari A, Vaziri-Moghaddam H, et al. (2016) Facies analysis and paleoenvironmental reconstruction of upper cretaceous sequences in the eastern Para-Tethys basin, NW Iran. *Geol Acta* 14: 363–384.
62. Baioumy H, Omran M, Fabritius T (2017) Mineralogy, geochemistry and the origin of high-phosphorus oolitic iron ores of Aswan, Egypt. *Ore Geol Rev* 80: 185–199.
63. Donnelly TH, Shergold JH, Southgate PN, et al. (1990) Events leading to global phosphogenesis around the Proterozoic-Cambrian transition, In: Notholt AJG, Jarvis I, *Phosphorite research and development*, London: Journal Geology Society London. Special Publication, 52: 273–287.
64. Trappe J (1998) *Phanerozoic phosphorite depositional systems: A dynamic model for a sedimentary resource system*, Lecture Notes in Earth Science 76: 1–316.
65. Piper DZ (1991) Geochemistry of a Tertiary sedimentary phosphate deposit: Baja California Sur, Mexico. *Chem Geol* 92: 283–316.
66. Soudry D, Ehrlich S, Yoffe O, et al. (2002) Uranium oxidation state and related variations in geochemistry of phosphorites from the Negev (southern). *Chem Geol* 189: 213–230.
67. Jarvis I, Burnett WC, Nathan Y, et al. (1994) Phosphorite geochemistry: state-of-the-art and environmental concerns. *Eclogae Geol Helv* 87: 643–700.

68. Garnit H, Bouhlel S, Jarvis I (2017) Geochemistry and depositional environments of Paleocene-Eocene phosphorites: Metlaoui Group, Tunisia. *J Afr Earth Sci* 134: 704–736.
69. McArthur JM (1985) Francolite geochemistry-compositional controls during formation, diagenesis, metamorphism and weathering. *Geochim Cosmochim Acta* 49: 23–35.
70. McArthur JM (1978) Systematic variations in the contents of Na, Sr, CO_2 and SO_4 in marine carbonate fluorapatite and their relation to weathering. *Chem Geol* 21: 41–52.
71. Altschuler ZS (1980) The geochemistry of trace elements in marine phosphorites. Part I: characteristic abundances and enrichment, In: Bentor YK, *Marine Phosphorites*, London: SEPM Special Publication, 29: 19–30.
72. Prévôt L (1990) Geochemistry, Petrography, Genesis of Cretaceous-Eocene Phosphorites. *Soc Geol Fr Mem* 158: 1–232.
73. Jiang SY, Zhao HX, Chen YQ, et al. (2007) Trace and rare earth element geochemistry of phosphate nodules from the lower Cambrian black shale sequence in the Mufu Mountain of Nanjing, Jiangsu province, China. *Chem Geol* 244: 584–604.
74. Prevot L, Lucas J (1980) Behaviour of some trace elements in phosphatic sedimentary formations. *Society of Economic Paleontologists and Mineralogists*, *Special Publication* 29: 31–40.
75. Gulbrandsen RA (1966) Chemical composition of the phosphorites of the Phosphoria Formation. *Geochim cosmochim Acta.* 30: 769–778.
76. Slansky M (1986) *Geology of sedimentary phosphate (Studies in Geology)*, 1st English edition, North Oxford Academic Publishers Limited, 59–159.
77. Iylin AV, Volkov RI (1994) Uranium Geochemistry in Vendian-Cambrian Phosphorites. *Geokhimiya* 32: 1042–1051.
78. Sokolov AS (1996) Evolution of Uranium Mineralization in Phosphorites. *Geokluntiva* 11:1117–1119.
79. Zanin YN, Zanrirailova AG, Gilinskaya LG, et al. (2000) Uranium in the Sedimentary Apatite during Catagenesis. *Geokhimiya* 5: 502–509.
80. Baturin GN, Kochenov AV (2001) Uranium in phosphorites. *Lithol Miner Resour* 36: 303–321.
81. Smirnov KM, Men'shikov YA, Krylova OK, et al. (2015) Form of Uranium Found in Phosphate Ores in Northern Kazakhstan. *At Energy* 118: 337–340.
82. Cunha CSM, da Silva YJAB, Escobar MEO, et al. (2018) Spatial variability and geochemistry of rare earth elements in soils from the largest uranium-phosphate deposit of Brazil. *Environ Geochem Health* 40: 1629–1643.
83. Lucas J, Prevot J, Larnboy M (1978) Les phosphorites de in marge norde de I' Espagne, Cl imie mineralogy, Genese. *Oceanol Acta* 1: 55–72.
84. Saigal N, Banerjee DM (1987) Proterozoic phosphorites of India: updated information. Part 1: Petrography, In: Kale VS, Phansalkar VG, *Purana Basins of Peninsular India*, India: Geological Society of India Memoir, 6: 471–486.
85. Dooley JH (2001) Baseline Concentrations of Arsenic, Beryllium and Associated Elements in Glauconite and Glauconitic Soils in the New Jersey Coastal Plain, *The New Jersey Geological Survey,* Investigation Report, Trenton NJ, 238.
86. Barringer JL, Reilly PA, Eberl DD, et al. (2011) Arsenic in sediments, groundwater, and stream water of a glauconitic Coastal Plain terrain, New Jersey, USA. *Appl Geochem* 26: 763–776.
87. Liu YG, Mia MRU, Schmitt RA (1988) Cerium: A chemical tracer for paleo oceanic redox conditions. *Geochim Cosmochim Acta* 52: 2362–2371.

88. German CR, Elderfield H (1990) Application of the Ce anomaly as a paleoredox indicator: the ground rules. *Paleoceanography* 5: 823–833.
89. Murray RW, Brink MRB, Ten Gerlach DC, et al. (1991) Rare earth, major, and trace elements in chert from the Franciscan Complex and Monterey Group, California: Assessing REE sources to fine-grained marine sediments. *Geochim Cosmochim Acta* 55: 1875–1895.
90. Nath BN, Roelandts I, Sudhakar M, et al. (1992) Rare Earth Element patterns of the Central Indian Basin sediments related to their lithology. *Geophys Res Lett* 19: 1197–1200.
91. Madhavaraju J, Ramasamy S (1999) Rare earth elements in Limestones of Kallankurichchi Formation of Ariyalur Group, Tiruchirapalli Cretaceous, Tamil Nadu. *J Geol Soc India* 54: 291–301.
92. Armstrong-Altrin JS, Verma SP, Madhavaraju J, et al. (2003) Geochemistry of Late Miocene Kudankulam Limestones, South India. *Int Geol Rev* 45: 16–26.
93. Madhavaraju J, González-León CM, Lee YI, et al. (2010) Geochemistry of the Mural Formation (Aptian-Albian) of the Bisbee Group, Northern Sonora, Mexico. *Cretac Res* 31: 400–414.
94. Wang YL, Liu YG, Schmitt RA (1986) Rare earth element geochemistry of South Atlantic deep sea sediments: Ce anomaly change at ~54 My. *Geochim Cosmochim Acta* 50: 1337–1355.
95. Kato Y, Nakao K, Isozaki Y (2002) Geochemistry of Late Permian to Early Triassic pelagic cherts from southwest Japan: implications for an oceanic redox change. *Chem Geol* 182: 15–34.
96. Kamber BS, Webb GE (2001) The geochemistry of late Archaean microbial carbonate: implications for ocean chemistry and continental erosion history. *Geochim Cosmochim Acta* 65: 2509–2525.
97. Kemp RA, Trueman CN (2003) Rare earth elements in Solnhofen biogenic apatite: geochemical clues to the palaeoenvironment. *Sediment Geol* 155: 109–127.
98. Bakkiaraj D, Nagendra R, Nagarajan R, et al. (2010) Geochemistry of Siliciclastic rocks of Sillakkudi Formation, Cauvery Basin, Southern India; Implications for Provenance. *J Geol Soc India* 76: 453–467.
99. McArthur JM, Walsh JN (1984) Rare-earth geochemistry of phosphorites. *Chem Geol* 47: 191–220.
100. Kidder DL, Krishnaswamy R, Mapes RH (2003) Elemental mobility in phosphatic shales during concretion growth and implications for provenance analysis. *Chem Geol* 198: 335–353.
101. Cossa M (1878) Sur la diffusion de cerium, du lanthane et du didyme, extract of a letter from Cossa to Sella, presented by Freny. *C R Ac Sci* 87: 378–388.
102. McKelvey VE (1967) *Rare Earths in Western Phosphate Rocks*. US Geological Survey Professional paper, 1–17.
103. Kocsis L, Gheerbrant E, Mouflih M, et al. (2016) Gradual changes in upwelled seawater conditions (redox, pH) from the late Cretaceous through early Paleogene at the northwest coast of Africa: negative Ce anomaly trend recorded in fossil bio-apatite. *Chem Geol* 421: 44–54.
104. Altschuler ZS, Berman S, Cuttiti F (1967) Rare earths in phosphorites-geochemistry and potential recovery, *U. S. Geological Survey Professional paper*, 575: 1–9.
105. Kon Y, Hoshino M, Sanematsu K, et al. (2014) Geochemical characteristics of apatite in heavy REE-rich deep-sea mud from Minami-Torishima area, southeastern Japan. *Resour Geol* 64: 47–57.
106. Taylor SR (1985) An examination of the geochemical record preserved in sedimentary rocks. In: Taylor SR, McLennan SM, *The Continental Crust; Its composition and evolution*, Blackwell, Oxford, 312.

107. Shields G, Stille P (2001) Diagenetic constraints on the use of cerium anomalies as palaeoseawater redox proxies: an isotopic and REE study of Cambrian phosphorites. *Chem Geo* 175: 29–48.
108. Elderfield H, Greaves MJ (1982) The rare earth elements in seawater. *Nature* 296: 214–219.
109. De Baar HJW, Bacon MP, Brewer PG (1985) Rare earth elements in the Pacific and Atlantic Oceans. *Geochim Cosmochim Acta* 49: 1943–1959.
110. Pattan JN, Pearce NJG, Mislankar PG (2005) Constraints in using Cerium-anomaly of bulk sediments as an indicator of paleo bottom water redox environment: A case study from the Central Indian Ocean Basin. *Chem Geol* 221: 260–278.
111. Daesslé LW, Carriquiry JD (2008) Rare Earth and Metal Geochemistry of Land and SubmarinePhosphorites in the Baja California Peninsula, Mexico. *Mar Georesour Geotechnol* 26: 340–349.
112. Stoneley R (1990) The Arabian continental margin in Iran during the late Cretaceous, In: Roberston AHF, Searl MP, Ries A, *The geology and tectonics of the Oman region*, London: Geological Society of London Special Publication, 49: 787–795.
113. Bolourchifard F, Fayazi F, Mehrabi B, et al. (2019) Evidence of high-energy storm and shallow water facies in Pabdeh sedimentary phosphate deposit, Kuhe-Lar-anticline, SW Iran. *Carbonate Evaporite* 34: 1703–1721.
114. Daneshian J, Shariati S, Salsani A (2015) Biostratigraphy and planktonic foraminiferal abundance in the phosphate bearing pabdeh Formation of the lar mountains (SW Iran). *Neues Jahrb Geol Paläontol* 278: 175–189.
115. Rees A, Thomas A, Lewis M, et al. (2014) Lithostratigraphy and palaeoenvironments of the Cambrian in SW Wales. *Geol Soc London* 42: 33–100.
116. Vaziri-Moghaddam H, Kimiagari M, Taheri A (2006) Depositional environment and sequence stratigraphy of the Oligo-MioceneAsmari Formationin SW Iran. *Facies* 52: 41–51.
117. Murris RJ (1980) Middle East: stratigraphic evolution and oil habitat. *Am Assoc Pet Geol Bull* 64: 597–618.
118. Price NB, Calvert SE (1978) The geochemistry of phosphorites from the Namibian shelf. *Chem Geol* 23: 151–170.
119. Froelich PN, Arthur MA, Burnett WC, et al. (1988) Early diagenesis in organic matter in Peru continental margin sediments: Phosphorite precipitation. *Mar Geol* 80: 309–343.
120. Tribovillard N, Algeo TJ, Lyons T, et al. (2006) Trace metals as paleoredox and paleoproductivity proxies: an update. *Chem Geol* 232: 12–32.
121. MacLeod KG, Irving AJ (1996) Correlation of cerium anomalies with indicators of paleoenvironment. *J Sediment Res* 66: 948–988.
122. Shields G, Stille P, Brasier MD, et al. (1997) Stratified oceans and oxygenation of the late Proterozoic environment: a post glacial geochemical record from the Neoproterozoic of W Mongolia. *Terra Nov* 9: 218–222.